International Communications in Heat and Mass Transfer 174 (2026) 110904

Contents lists available at ScienceDirect

International Communications in Heat and Mass Transfer

journal homepage: www.elsevier.com/locate/ichmt

A novel biogas combustion-heat recovery for cooling/power co-production system considering a modified sCO_2 cycle and a generator-absorber-exchanger (GAX) cycle: Machine learning-driven optimization and economic study

Zhongkui Zhang [a], Ling Yao [b,*], Khalid Alkhattabi [c], Omar J. Alkhatib [d,*], Ashit Kumar Dutta [e,f], Hind Albalawi [g], H. Elhosiny Ali [h,i], Ibrahim Mahariq [j,k,l,m,n,*]

[a] School of Mechanical and Electrical Engineering, Weifang University of Science and Technology, Weifang 262700, China
[b] School of Electronic Engineering and Intelligent Manufacturing, Anhui Xinhua University, Hefei 230088, China
[c] College of Computers and Information Technology, University of Tabuk, Tabuk 47512, Saudi Arabia
[d] Architectural Engineering Department, United Arab Emirates University Al Ain, United Arab Emirates
[e] Department of Computer Science and Information Systems, College of Medical Sciences, AlMaarefa University, Dariyah, 13713, Saudi Arabia
[f] Research Center, Deanship of Scientific Research and Post-Graduate Studies, AlMaarefa University, Dariyah, 13713, Saudi Arabia
[g] Department of Physics, College of Sciences, Princess Nourah bint Abdulrahman University, P.O. Box 84428, Riyadh 11671, Saudi Arabia
[h] Central Labs, King Khalid University, AlQura'a, Abha, P.O. Box 960, Saudi Arabia
[i] Physics Department, Faculty of Science, King Khalid University, P.O. Box 9004, Abha, Saudi Arabia
[j] College of Engineering and Architecture, Gulf University for Science and Technology, Mishref, Kuwait
[k] Department of Electrical and Electronic Engineering, Faculty of Engineering and Architecture, Istanbul Gelisim University, Avcılar- Istanbul, 34310, Istanbul, Türkiye
[l] Najjad Zeenni Faculty of Engineering, Al-Quds University, Jerusalem, Palestine
[m] Department of Medical Research, China Medical University Hospital, China Medical University, Taichung, Taiwan
[n] University College, Korea University, Seoul 02481, South Korea

ARTICLE INFO

Keywords:
Heat recovery systems
GAX cooling cycle
Combined cooling and power (CCP)
Thermodynamic–financial analysis
Biogas utilization
Machine learning optimization

ABSTRACT

Biogas-driven combined cooling and power (CCP) systems face the challenge of simultaneously optimizing thermodynamic performance and financial viability under nonlinear design and operational constraints. This study proposes a novel biogas combustion–heat recovery configuration for CCP generation, evaluated through an integrated thermodynamic–financial framework and optimized using machine learning (ML)-driven soft-computing techniques. The system integrates a biogas combustion unit, a gas turbine, a modified supercritical CO_2 cycle, and a generator–absorber–exchanger (GAX) cycle. Thermodynamic analyses based on the first and second laws of thermodynamics are employed, while sustainability, financial, and environmental indicators are incorporated into the assessment. A hybrid optimization approach, combining ML with the genetic algorithm optimizer, is implemented to accelerate convergence and explore trade-offs among net present value (NPV), total unit product cost (TUPC), and sustainability index (SI). The optimized configuration achieves an NPV of 13.03 M $, an SI of 1.765, and a TUPC of 26.5 $/GJ. Besides, the system demonstrates an energy efficiency of 62.75%, an exergy efficiency of 43.32%, and a payback period of 3.79 years, confirming technical robustness and economic viability. Overall, ML-driven soft computing enables resilient, investment-ready CCP strategies, offering a scalable plan that aligns biogas utilization with sustainability, efficiency, and competitiveness.

1. Introduction

The rapid growth in global energy demand has historically been met through extensive reliance on fossil fuels such as coal, oil, and natural gas [1,2]. While these resources have driven industrial development and urban expansion, their combustion is directly associated with severe environmental consequences, including greenhouse gas emissions, air pollution, and long-term climate change [3,4]. In addition, the finite nature of fossil reserves raises concerns about energy security and

* Corresponding authors at: Najjad Zeenni Faculty of Engineering, Al-Quds University, Jerusalem, Palestine
E-mail addresses: yaoling@axhu.edu.cn (L. Yao), omar.alkhatib@uaeu.ac.ae (O.J. Alkhatib), mahariq@korea.ac.kr (I. Mahariq).

https://doi.org/10.1016/j.icheatmasstransfer.2026.110904

Available online 25 February 2026

Nomenclature

A	Area (m^2)
AB	Air blower
AI	Annual income ($)
ANN	Artificial neural network
AS	Annual savings ($)
$\dot{C}$	Cost rate ($/h)
c	Unit exergy cost ($/GJ)
CC	Combustion chamber; Cooling capacity
CCP	Combined cooling and power
CCHP	Combining cooling, heating, and power
CEPCI	Chemical engineering plant cost index
CO_2ER	CO_2 emission rate (kg/kWh)
CRF	Capital recovery factor
D_p	Depletion factor
e	Specific exergy (kJ/kg)
EE	Exergy efficiency (%)
$\dot{E}$	Exergy rate (kW)
FA	Fuel to air ratio
FC	Fixed cost ($)
GAX	Generator–absorber–exchanger
GT	Gas turbine
h	Specific enthalpy (kJ/kg)
i_r	Annual interest rate (%)
IF	Inflation factor
m_{NOx}	NOx emissions (g/kg fuel)
m_{CO}	CO emissions (g/kg fuel)
$\dot{m}$	Mass flow rate (kg/s)
ML	Machine learning
MSC	Modified supercritical CO_2
(n)	Lifetime (years)
N	Operational time (h)
(NPV)	Net present value ($)
NSGA-II	Non-dominated sorting genetic algorithm-II
LHV	Lower heating value (kJ/kg)
OC	Operating cost ($)
P	Pressure (kPa)
PP	Payback period (year)
($\dot{Q}$)	Heat rate (kW)
RDF	Real discount factor
SI	Sustainability index
s	Specific entropy (kJ/kg.K)
T	Absolute temperature (K)
T_{pz}	Adiabatic flame temperature (K)
TE	Thermal efficiency (%)
TUPC	Total unit product cost ($/GJ)
V	Voltage (V)
($\dot{W}$)	Electricity (kW)
y	Molar fraction (−)
Z	Purchase cost ($)
$\dot{Z}$	Cost rate of investment ($/h)

Greek symbols

η	Efficiency (%)
ε	Effectiveness (%)
Π	Pressure dimensionless
Θ	Temperature dimensionless
Ψ	H/C atomic ratio
τ	Primary zone residence time (s)
φ	Maintenance factor

Subscripts

ch	Chemical
des	Destruction
ex	Exergy
F	Fuel
is	Isentropic
in	Inlet
L	Loss
out	Outlet
P	(Product)
ph	(Physical)
PY	Present year
RY	Reference year
th	Thermal
tot	Total

sustainability for future generations [5]. These drawbacks highlight the urgent need to transition toward renewable energy sources as integral components of modern energy management strategies, particularly within urban environments where demand density and environmental pressures are highest [6,7]. Among the diverse portfolio of renewable options, biogas offers a promising pathway due to its carbon-mitigating potential, availability from waste-to-energy processes, and ability to support decentralized power generation [8,9]. Beyond simple energy recovery, the combustion of biogas becomes especially valuable when integrated into multi-functional systems that simultaneously generate electricity, heating, and cooling [10]. Such integrated biogas-based systems not only improve energy utilization efficiency but also contribute to sustainable urban energy infrastructures that align environmental stewardship with economic competitiveness [11].

Arslan and Yilmaz et al. [12] investigated the conversion of a biogas power plant into a trigeneration system combining cooling, heating, and power (CCHP) units. Energy, exergy, and cost analyses showed that exergy efficiency increased to 50.14%, while unit costs for heating and cooling decreased to 0.0178 $/kWh and 0.0352 $/kWh, respectively. Castley et al. [13] modeled a CCHP system fueled by cattle manure in an anaerobic digestion reactor (ADR) with biogas upgrading. Eight configurations were simulated and optimized for an office building in a heating-dominated European climate, achieving a performance index of 151.1%, a 93.7% reduction in carbon emissions, and 32.0% primary energy savings. Ebadollahi et al. [14] analyzed a biogas-driven combined power system coupling Brayton and Rankine cycles through thermodynamic, exergoeconomic, and exergoenvironmental assessments. The system produced 1372 kW net power, with 37.57% energy efficiency, 21.27% exergy efficiency, and a unit cost of 21.46 $/GJ. Herve et al. [15] studied a biogas–syngas co-firing CCHP system integrating a gasification unit, an internal combustion engine (ICE), and an organic Rankine cycle (ORC). Aspen Plus simulations showed that energy efficiency declined with higher methane content, whereas exergy efficiency improved at 80–90% extraction rates. Increasing the gasification temperature enhanced performance, while a higher biogas temperature reduced efficiency. Anand et al. [16] proposed a hybrid system combining biogas, photovoltaics (PV), and a battery energy storage system with a fuel cell stack. A heuristic power management system and artificial neural network (ANN)-based digester control were applied, achieving 28.42% cost savings and 96% carbon emission reduction. Tian et al. [17] developed a biogas-fueled CCHP system comprising ORCs, heat exchangers, and an ammonia–water absorption chiller. Aspen Hysys simulations reported 61% energy efficiency and 30.44% exergy efficiency, with the biogas burner accounting for 87.4% of exergy

destruction. The system emitted 0.293 kg_{CO_2}/kWh, had a product cost of 0.017 $/kWh, and a payback period of 6.11 years. Gholizadeh et al. [18] introduced a biogas–liquefied natural gas (LNG) cogeneration system integrating open- and closed-loop Brayton cycles, an ORC, and an ejector refrigeration cycle. Multi-objective optimization showed 1860 kW electricity, 427.3 kW cooling, 80.79% energy efficiency, 41.5% exergy efficiency, a 48% reduction in carbon emissions, and a unit product cost of 9.81 $/GJ. Huang et al. [19] investigated a biogas-driven CCHP system with chemical reinjection to improve methane conversion and heat integration. The system achieved 55.52 kW (6.2%) higher electricity, 542.49 kW (101.5%) higher cooling, and an 8.31% increase in exergy efficiency, with reduced irreversibilities. Haghghi et al. [20] proposed an oxy-combustion polygeneration system fueled by biogas, integrating a supercritical CO_2 Brayton cycle, an ammonia–water combined cooling and power (CCP) unit, a multi-effect desalination unit, and a Rankine cycle. Optimization yielded 1644 kW electricity, 44.71 kW cooling, 41.81 kW heating, and 66.35 m^3/day water, achieving 49.32% exergy efficiency and 27.54 $/GJ unit cost. Finally, Feili et al. [21] presented a biogas-based multi-integrated system combining an S-Graz cycle, a steam reforming unit, and a methanol synthesis unit. Hybrid optimization yielded 3.25 m^3/h methanol at 0.5771 $/kg, with 46.5% exergetic efficiency and a 4.77-year payback period, demonstrating efficient methanol and electricity co-production. Athari et al. [22] investigated thermodynamic and exergoeconomic performance of biomass gasification-based power plants, comparing externally fired, co-firing, and post-firing combined cycle configurations. The post-firing system was identified as the most economically effective, achieving higher energy efficiency. Qeshmi et al. [23] analyzed a biomass-powered multigeneration system producing electricity, heating, cooling, hydrogen, and freshwater using exergy, exergoeconomic, and exergoenvironmental approaches. The gasifier and heat exchanger were identified as major sources of exergy destruction, highlighting economic–environmental trade-offs. Laleh et al. [24] proposed a biogas-fueled multigeneration system integrating oxy-fuel combustion, thermochemical hydrogen production, ORC, and thermophotovoltaic power generation. Thermodynamic, economic, and environmental analyses combined optimization demonstrated high exergetic efficiency, reduced product cost, and improved environmental performance. Rabet et al. [25] developed a multigeneration system combining biomass digestion, gasification, geothermal energy, Kalina cycle, and desalination technologies. Thermodynamic and exergoeconomic analyses showed moderate second law efficiency, with major exergy destruction occurring in desalination units.

Cooling is a fundamental aspect of engineering systems, essential for maintaining safe operating temperatures, improving efficiency, and extending equipment lifespan [26–28]. In addition to power generation, the growing demand for cooling in residential, commercial, and industrial sectors underscores the importance of integrating cooling subsystems into multi-generation energy systems [29,30]. Traditional cooling technologies are often electricity-intensive, thereby increasing peak loads on urban grids and reducing overall system efficiency [31]. By contrast, thermally driven cooling technologies enable the direct use of waste heat, improving resource utilization and reducing reliance on conventional electricity-based cooling. Among these, the generator–absorber–exchanger (GAX) cycle has gained attention for its high efficiency, ability to operate with low-grade thermal energy, and compatibility with renewable-fueled systems [32]. The GAX cycle not only reduces primary energy consumption but also enhances overall system sustainability by coupling power and heat recovery with effective cooling generation [33]. Haghghi et al. [34] evaluated a multigeneration structure integrating a molten carbonate fuel cell (MCFC), a superheated steam heat exchanger, a GAX cycle for cooling, and a desalination unit. The system achieved 79.9% energy efficiency, 51.9% exergy efficiency, 21.6 $/GJ unit exergy cost, and 247 kg_{CO_2}/MWh emissions, demonstrating efficient cooling generation alongside electricity and freshwater production. Salehi et al. [35] analyzed a trigeneration system combining a MCFC, a Stirling engine, a heat recovery steam generator, and GAX and vapor absorption refrigeration cycles. Utilizing the GAX cycle for cooling, the system reached 52.12% exergy efficiency and 0.358 t/MWh CO_2 emissions, confirming effective cooling generation and favorable thermodynamic and environmental performance. Seiiedhoseiny et al. [36] investigated a high-efficiency multigeneration structure powered by geothermal energy, integrating a single-flash cycle, branched GAX cooling cycle, and an electrolyzer. Optimization results included 36.82% energy efficiency, 65.42% exergy efficiency, 7.046 $/GJ unit cost, 4187 kW net electricity, and 5.85 kg/h hydrogen production, demonstrating low-cost multigeneration performance with effective cooling. Jia et al. [37] proposed a hybrid absorption–compression heat pump, incorporating GAX-based internal heat recovery to exploit low-temperature heat sources. The system achieved a coefficient of performance above 1.61, a primary energy ratio above 1.11, and a temperature lift up to 85.9 °C, enabling efficient space heating even at −40.6 °C and integration with solar collectors. Jawahar [38] examined an ammonia–water absorption refrigeration system with a GAX cycle. MATLAB simulations showed that adding Al_2O_3 nanoparticles improved system performance by 15–20% compared to the conventional cycle, enhancing cooling efficiency.

According to the literature, utilizing biogas for multigeneration systems represents a sustainable and efficient approach to energy production, particularly for urban energy management. Such systems are especially valuable in urban environments, where high energy demand and the need for environmentally responsible solutions require compact, high-performance, and cost-effective energy infrastructures. Despite advances in renewable energy technologies, the research gaps identified in the literature review include:

- Limited attention has been paid to the simultaneous thermodynamic and financial optimization of biogas-fueled multigeneration systems, particularly those incorporating advanced cooling technologies.
- Most prior research on biogas utilization does not adequately address integrated cooling generation, and thermally driven advanced cycles have been insufficiently explored.
- The GAX cycle has rarely been investigated in integration with biogas combustion-based arrangements.
- Optimization methodologies applied in previous works are predominantly conventional, with minimal use of hybrid soft-computing or machine learning (ML)–assisted frameworks.
- Few studies adopt a holistic ML–evolutionary optimization approach capable of effectively navigating nonlinear, multi-objective thermodynamic–financial design spaces while preserving solution diversity.

With regard to these gaps, the main novel aspects of the paper are:

- This study proposes a novel biogas-based multi-generation system that couples a GT with a modified supercritical CO_2 (MSC) cycle and a GAX cooling cycle.
- The proposed configuration enables the simultaneous utilization of high- and low-grade thermal energy, enhancing overall system efficiency.
- The proposed configuration integrates sustainable system design principles by aligning thermodynamic performance with financial feasibility, ensuring that the solution is energy-efficient, investment-ready, and suitable for real-world deployment.
- A hybrid ML-driven soft-computing optimization framework is developed by coupling ML models with the non-dominated sorting genetic algorithm-II (NSGA-II) algorithm to improve convergence speed, solution accuracy, and diversity.
- The study uniquely combines advanced thermodynamic cycles with data-driven optimization in a biogas-fueled multigeneration context.

The objectives of this research are to design a biogas-driven CCP

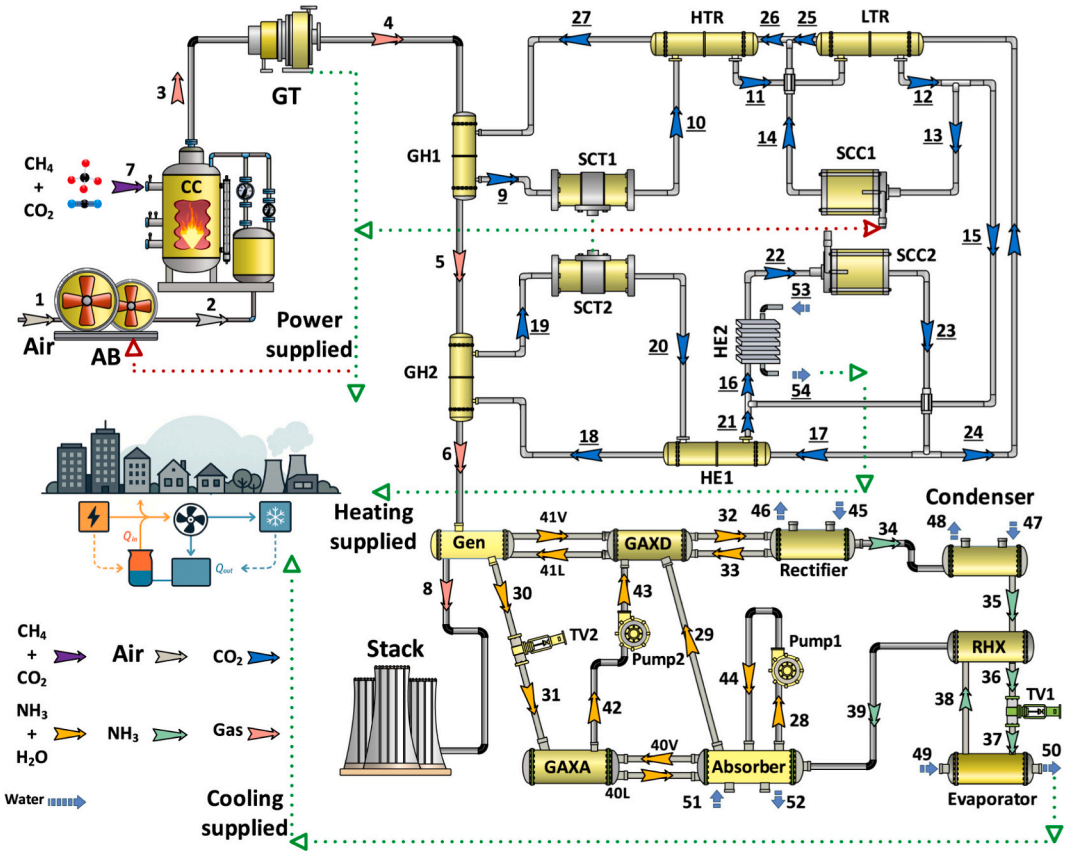

Fig. 1. The schematic plot of the planned biogas-driven system in this study.

system, perform a comprehensive thermodynamic and exergy analysis, and evaluate financial feasibility using metrics such as net present value (NPV), total unit product cost (TUPC), and payback period (PP). The study also assesses sustainability performance through exergy efficiency and a sustainability index (SI), develops the hybrid ML-driven optimization framework to handle complex multi-objective trade-offs, and identifies optimal operating and design conditions that maximize thermodynamic performance while ensuring financial viability and environmental benefits.

2. System description

The proposed system integrates a biogas-fired GT with a MSC cycle and a GAX refrigeration cycle to maximize energy utilization, efficiency, and economic feasibility (Fig. 1). The use of biogas as a renewable fuel for GTs has been increasingly adopted worldwide in recent years, providing a carbon-mitigating and reliable power source. The MSC cycle is incorporated to recover high-grade waste heat from the GT exhaust, converting it into additional electricity with minimal irreversibility, while the GAX cycle exploits low-grade heat to produce cooling, enhancing the overall sustainability of the system. This configuration is supported by extensive experimental studies and real-world applications of MSC and absorption refrigeration cycles, demonstrating their feasibility when coupled with GTs. Considering the thermodynamic conditions of the GT exhaust, the staged heat recovery through the MSC and GAX cycles is fully justified, enabling multi-level energy extraction and improved system performance.

As shown in Fig. 1, biogas enters the combustion chamber (CC) at state 7, where it is burned with pressurized air supplied by the air blower (AB) at state 2. The combustion products exit the CC at state 3 and expand through the GT, generating power for the grid. The turbine exhaust at state 4 is then directed to the MSC cycle for heat recovery.

Within the MSC cycle, CO_2 leaving the high-temperature recuperator (HTR) at state 27 is further heated in gas heater 1 (GH1) before expansion in SC's turbine 1 (SCT1), producing additional power. The exhaust from SCT1 at state 10 undergoes sequential heat recovery in the HTR and the low-temperature recuperator (LTR), exiting at state 11. At state 12, the flow is divided: stream 13 is compressed in SC's compressor 1 (SCC1) to state 14, while stream 15 proceeds to the bottoming section of the MSC cycle. In the second section, stream 18 is heated in GH2 and expanded in SCT2 at state 19 to produce further power. The turbine exhaust at state 20 transfers heat via exchanger HE1 to preheat stream 18, before mixing with stream 15 at state 21. The combined stream 16 flows into HE2 and is cooled down. Stream 22 is compressed in SCC2 to state 23 and split into two streams: stream 17, which continues circulation, and stream 24, which passes through the LTR to reach state 25. After mixing with stream 14, stream 26 enters the HTR, closing the cycle as stream 27.

Finally, the hot exhaust leaving GH2 at state 6 is directed to the GAX cycle, where it drives the third stage of heat recovery to produce the cooling load. In the GAX cycle, an ammonia–water mixture is employed as the working fluid. The saturated weak solution with relatively higher refrigerant concentration exits the absorber at state 28 and is pumped toward the generator, passing through solution heat exchangers that recover heat from both the absorber's high-temperature section and the GAXD. Inside the generator, this solution undergoes boiling, producing a vapor stream (state 41 V) enriched with ammonia. The remaining weak solution (state 30) leaves the generator, flows through throttling valve 2 (TV2), and enters the GAXA at state 31, where it releases heat to the solution discharged by the pump before returning to the absorber. Meanwhile, the ammonia-rich vapor from the generator proceeds through the GAXD (state 32) and the rectifier (state 34), where its ammonia concentration is further increased, resulting in the nearly pure vapor stream at state 35. The liquid condensed in the rectifier (state 33)

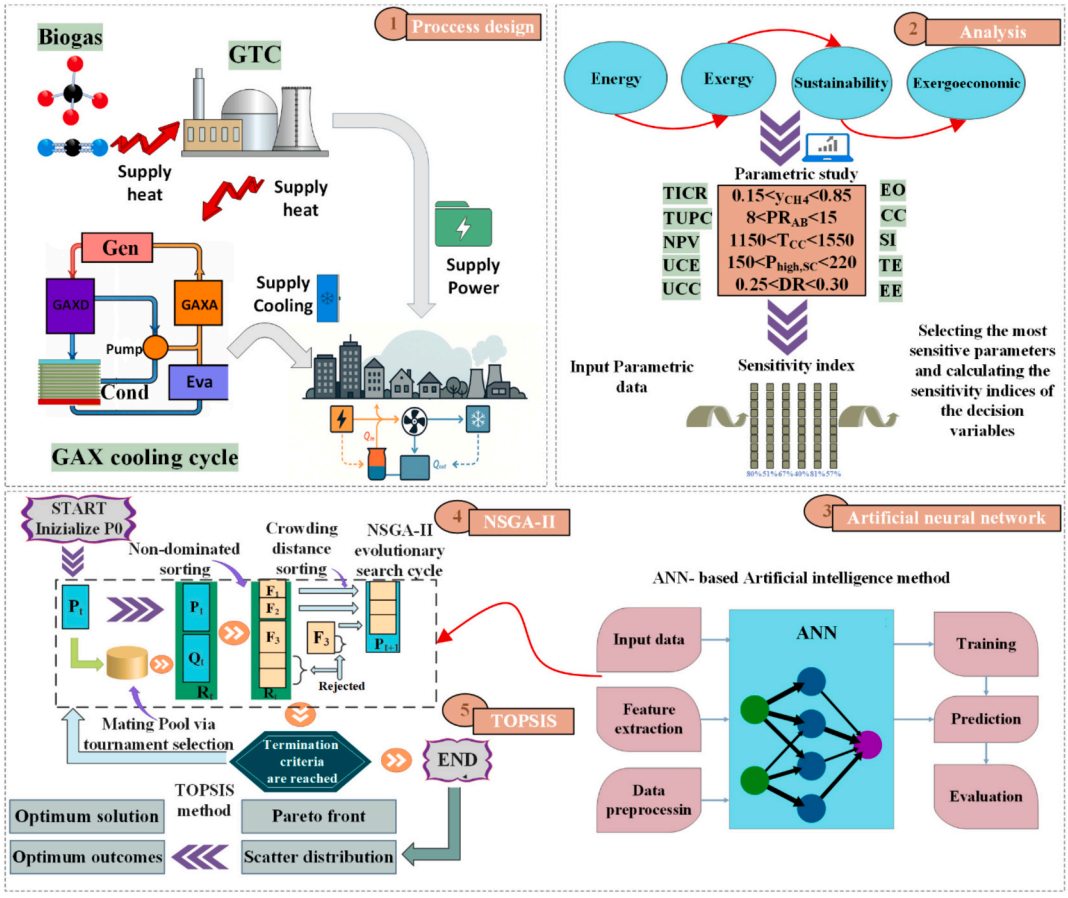

Fig. 2. The processes of simulations, analyses, and optimization conducted in this study.

Table 1
Initial input design parameters.

Biogas combustion and GT section [39,40]		*GAX cycle* [41,42]	
Parameters	value	NH_3 mass fraction at rectifier outlet, $X_{out,rect}$	0.995
AB pressure ratio, PR_{AB} (−)	10*	Degassing range, DR	0.25*
CC operating temperature, T_{CC} (K)	1300*	Generator's outlet temperature,T_{gen} (K)	420
Methane molar fraction, y_{CH4} (−)	0.6*	Absorber's outlet temperatures, T_{abs}(K)	309
AB isentropic efficiency, η_{AB} (%)	86	Evaporator's outlet temperatures, T_{eva}(K)	278.15
GT isentropic efficiency, η_{GT} (%)	86	Condenser's outlet temperature, T_{cond}(K)	313
Electricity production capacity, $\dot{W}_{net,GT}$ (kW)	1000	Inlet cooling water temperature,$T_{in,water}$(K)	293.2
MSC cycle [43]		Evaporator's outlet quality, $Qu_{out,eva}$	0.94
Low pressures of SC cycle, $P_{low,SC}$ (bar)	74	Pumps isentropic efficiency, η_{pums} (%)	50
High pressures of SC cycle, $P_{high,SC}$ (bar)	220	*General system assumptions*	
Mass ratio, MSR = $\dot{m}_{24}/\dot{m}_9$	0.83	Dead state pressure, P_0 (kPa)	101.3
Effectiveness HTR and LTR, $\varepsilon_{HTR,LTE}$ (−)	0.86	Dead state temperature, T_0 (k)	293.2
Effectiveness GHs, ε_{GHs} (−)	0.90	Pressure drop in CC, ΔP_{CC} (%)	4
SCCs isentropic efficiency, η_{SCCs} (%)	0.85	Pressure drop in HEs, ΔP_{HEs} (%)	2
SCTs isentropic efficiency, η_{SCTs} (%)	0.90		

is directed back to the generator via the GAXD as stream 41 L. The purified liquid ammonia (state 35) passes through exchanger HE3, where it is precooled by the vapor stream leaving the evaporator (state 38). It is then throttled through valve TV1 to evaporator pressure (state 37), producing the cooling load at state 50. The low-pressure ammonia vapor generated in the evaporator (state 38) is subsequently absorbed by the weak solution entering the absorber from the GAXA, thus completing the cycle.

3. Methods

This study employs a combined thermodynamic, economic, and optimization framework to evaluate the performance of the proposed multigeneration system. The modeling and simulations were carried out using engineering equation solver (EES) to perform detailed energy, exergy, sustainability, and exergoeconomic analyses. The energy analysis determines the overall efficiency and distribution of energy streams, while the exergy analysis quantifies the quality of energy conversion and highlights the main sources of irreversibility. A sustainability assessment was included to measure the long-term viability of the system from the exergy perspective, and an exergoeconomic evaluation was conducted to link thermodynamic inefficiencies with their associated costs, providing insight into the system's economic competitiveness.

To further enhance system performance, ANN modeling was

Table 2
Each component's mass, energy, and exergy balance equations.

Component	Mass and energy balance equation	Exergy balance equation
Biogas combustion and GT section		
Air blower	$\dot{W}_{AB} = \dot{m}_1(h_2 - h_1)$, $\eta_{AB} = \frac{h_1 - h_{2s}}{h_1 - h_2}$; $\dot{m}_2 = \dot{m}_1$	$\dot{E}_{des,AB} = \dot{W}_{AB} - (\dot{E}_2 - \dot{E}_1)$
Combustion chamber	$-0.02\lambda\,\overline{LHV} + \bar{h}_{air} + \lambda\bar{h}_{fuel} - (1+\lambda)\bar{h}_{prod} = 0$, $\dot{Q}_{cc} = \dot{m}_{fuel}LHV$, $\dot{m}_3 = \dot{m}_7 + \dot{m}_2$	$\dot{E}_{des,CC} = (\dot{E}_2 + \dot{E}_7) - \dot{E}_3$
Gas turbine	$\dot{W}_{GT} = \dot{m}_4(h_4 - h_5)$, $\eta_{GT} = \frac{h_4 - h_5}{h_4 - h_{5S}}$; $\dot{m}_3 = \dot{m}_4$	$\dot{E}_{des,GT} = \left(\dot{E}_3 - \dot{E}_4\right) - \dot{W}_{GT}$
MSC cycle		
Gas heater1	$\dot{m}_4(h_4 - h_5) = \dot{m}_9(h_{27} - h_9)$; $\dot{m}_4 = \dot{m}_5$; $\dot{m}_9 = \dot{m}_{27}$	$\dot{E}_{des,GH1} = \left(\dot{E}_4 - \dot{E}_5\right) - \left(\dot{E}_9 - \dot{E}_{27}\right)$
Gas heater2	$\dot{m}_5(h_5 - h_6) = \dot{m}_{19}(h_{19} - h_{18})$; $\dot{m}_5 = \dot{m}_6$; $\dot{m}_{19} = \dot{m}_{18}$	$\dot{E}_{des,GH2} = \left(\dot{E}_5 - \dot{E}_6\right) - \left(\dot{E}_{19} - \dot{E}_{18}\right)$
HTL	$\dot{m}_{10}(h_{10} - h_{11}) = \dot{m}_{27}(h_{27} - h_{26})$; $\dot{m}_{10} = \dot{m}_{11}$; $\dot{m}_{27} = \dot{m}_{26}$	$\dot{E}_{des,HTL} = \left(\dot{E}_{10} - \dot{E}_{11}\right) - \left(\dot{E}_{26} - \dot{E}_{27}\right)$
LTL	$\dot{m}_{11}(h_{11} - h_{12}) = \dot{m}_{24}(h_{25} - h_{24})$; $\dot{m}_{11} = \dot{m}_{12}$; $\dot{m}_{24} = \dot{m}_{25}$	$\dot{E}_{des,LTR} = \left(\dot{E}_{11} - \dot{E}_{12}\right) - \left(\dot{E}_{25} - \dot{E}_{24}\right)$
Heat exchanger1	$\dot{m}_{20}(h_{20} - h_{21}) = \dot{m}_{18}(h_{18} - h_{17})$; $\dot{m}_{20} = \dot{m}_{21}$; $\dot{m}_{18} = \dot{m}_{17}$	$\dot{E}_{des,HE1} = \left(\dot{E}_{20} - \dot{E}_{21}\right) - \left(\dot{E}_{18} - \dot{E}_{17}\right)$
Heat exchanger2	$\dot{m}_{16}(h_{16} - h_{22}) = \dot{m}_{54}(h_{54} - h_{53})$; $\dot{m}_{16} = \dot{m}_{22}$; $\dot{m}_{54} = \dot{m}_{53}$	$\dot{E}_{des,HE2} = \left(\dot{E}_{16} - \dot{E}_{22}\right) - \left(\dot{E}_{54} - \dot{E}_{53}\right)$
SCT1	$\dot{W}_{SCT1} = \dot{m}_9(h_9 - h_{10})$, $\eta_{SCT1} = \frac{h_9 - h_{10}}{h_9 - h_{10S}}$; $\dot{m}_9 = \dot{m}_{10}$	$\dot{E}_{des,SCT1} = \left(\dot{E}_9 - \dot{E}_{10}\right) - \dot{W}_{SCT1}$
SCT2	$\dot{W}_{SCT2} = \dot{m}_{19}(h_{19} - h_{20})$, $\eta_{SCT2} = \frac{h_{19} - h_{20}}{h_{19} - h_{20S}}$; $\dot{m}_{19} = \dot{m}_{20}$	$\dot{E}_{des,SCT2} = \left(\dot{E}_{19} - \dot{E}_{20}\right) - \dot{W}_{SCT2}$
SCC1	$\dot{W}_{SCC1} = \dot{m}_{13}(h_{14} - h_{13})$, $\eta_{SCC1} = \frac{h_{14} - h_{13}}{h_{14} - h_{13S}}$; $\dot{m}_{14} = \dot{m}_{13}$	$\dot{E}_{des,SCC1} = \dot{W}_{SCC1} - (\dot{E}_{14} - \dot{E}_{13})$
SCC2	$\dot{W}_{SCC2} = \dot{m}_{23}(h_{23} - h_{22})$, $\eta_{SCC2} = \frac{h_{23} - h_{22}}{h_{23} - h_{22S}}$; $\dot{m}_{23} = \dot{m}_{22}$	$\dot{E}_{des,SCC2} = \dot{W}_{SCC2} - (\dot{E}_{23} - \dot{E}_{22})$
GAX cycle		
Absorber	$\dot{m}_{31} + \dot{m}_{39} = \dot{m}_{42} + \dot{m}_{28}$ $\dot{m}_{31}x_{31} + \dot{m}_{39}x_{39} = \dot{m}_{42}x_{42} + \dot{m}_{28}x_{28}$ $\dot{m}_{31}h_{31} + \dot{m}_{39}h_{39} + \dot{m}_{44}h_{44} = \dot{m}_{42}h_{42} + \dot{m}_{28}h_{28} + \dot{m}_{29}h_{29} + \dot{Q}_{abs,total}$	
GAXA	$\dot{m}_{42} + \dot{m}_{40L} = \dot{m}_{31} + \dot{m}_{40V}$ $\dot{m}_{42}x_{42} + \dot{m}_{40L}x_{40L} = \dot{m}_{31}x_{31} + \dot{m}_{40V}x_{40V}$ $\dot{m}_{42}h_{42} + \dot{m}_{40L}h_{40L} + \dot{Q}_{available} = \dot{m}_{31}h_{31} + \dot{m}_{40v}h_{40v}$	$\dot{E}_{des,gen\&abs} = \left(\dot{E}_6 - \dot{E}_8\right) - \left(\dot{E}x_{30} + \right.$ $\left. + \dot{E}_{32} + \dot{E}x_{42} + \dot{E}_{28} + \dot{E}_{52} - \dot{E}_{43} - \dot{E}_{33} - \dot{E}_{31} - \dot{E}_{44} - \dot{E}_{51} - \dot{E}_{29}\right)$
Generator	$\dot{m}_{30}h_{30} + \dot{m}_{32}h_{32} - \dot{Q}_{gen,total} = \dot{m}_{33}h_{33} + \dot{m}_{43}h_{43} + \dot{m}_{29}h_{29}$	
GAXD	$\dot{m}_{43} + \dot{m}_{41V} + \dot{m}_{29} + \dot{m}_{33} = \dot{m}_{32} + \dot{m}_{41L}$ $\dot{m}_{43}x_{43} + \dot{m}_{41V}x_{41V} + \dot{m}_{29}x_{29} + \dot{m}_{33}x_{33} = \dot{m}_{32}x_{32} + \dot{m}_{41L}x_{41L}$ $\dot{m}_{43}h_{43} + \dot{m}_{41V}h_{41V} + \dot{m}_{29}h_{29} + \dot{m}_{33}h_{33} + \dot{Q}_{required} = \dot{m}_{32}h_{32} + \dot{m}_{41L}h_{41L}$	
Heat exchanger3	$\dot{m}_{38} = \dot{m}_{39} = \dot{m}_{36} = \dot{m}_{35}$ $\dot{m}_{35}(h_{35} - h_{36}) = \dot{m}_{38}(h_{39} - h_{38})$, $\epsilon_{HE3} = \frac{T_{35} - T_{36}}{T_{35} - T_{38}}$	$\dot{E}_{des,HE3} = \left(\dot{E}_{35} - \dot{E}_{36}\right) - \left(\dot{E}_{39} - \dot{E}_{38}\right)$
Condenser	$\dot{m}_{34}(h_{34} - h_{35}) = \dot{m}_{48}(h_{48} - h_{47})$; $\dot{m}_{34} = \dot{m}_{35}$ $\dot{m}_{48} = \dot{m}_{47}$	$\dot{E}_{des,cond} = \left(\dot{E}_{35} - \dot{E}_{36}\right) - \left(\dot{E}_{48} - \dot{E}_{47}\right)$
Evaporator	$\dot{m}_{38} = \dot{m}_{37}$, $\dot{m}_{49} = \dot{m}_{50}$; $\dot{Q}_{eva} = \dot{m}_{38}(h_{38} - h_{37})$, $\dot{Q}_{eva} = \dot{m}_{49}(h_{49} - h_{50})$	$\dot{E}_{des,eva} = \left(\dot{E}_{37} - \dot{E}_{38}\right) - \left(\dot{E}_{50} - \dot{E}_{49}\right)$
Rectifier	$\dot{m}_{34} + \dot{m}_{33} = \dot{m}_{32}$, $\dot{m}_{45} = \dot{m}_{46}$; $\dot{m}_{32}x_{32} + \dot{m}_{33}x_{33} = \dot{m}_{34}x_{34}$ $\dot{m}_{46}(h_{46} - h_{45}) = \dot{m}_{32}h_{32} - \dot{m}_{33}h_{33} - \dot{m}_{34}h_{34}$	$\dot{E}_{des,rect} = \left(\dot{E}_{32} - \dot{E}_{34} - \dot{E}_{33}\right) - \left(\dot{E}_{46} - \dot{E}_{45}\right)$
Pump1	$\dot{W}_{pump1} = \dot{m}_{44}(h_{44} - h_{28})$, $\eta_{pumps} = \frac{h_{28} - h_{44s}}{h_{28} - h_{44}}$; $\dot{m}_{44} = \dot{m}_{28}$	$\dot{E}_{des,pump1} = \dot{W}_{pump1} - (\dot{E}_{44} - \dot{E}_{28})$
Pump2	$\dot{W}_{pump2} = \dot{m}_{43}(h_{43} - h_{42})$, $\eta_{pumps} = \frac{h_{42} - h_{43s}}{h_{42} - h_{43}}$; $\dot{m}_{43} = \dot{m}_{42}$	$\dot{E}_{des,pump2} = \dot{W}_{pump2} - (\dot{E}_{43} - \dot{E}_{42})$
TV1	$h_{36} = h_{37}$; $\dot{m}_{36} = \dot{m}_{37}$	$\dot{E}_{des,TV1} = \dot{E}_{36} - \dot{E}_{37}$
TV2	$h_{30} = h_{31}$; $\dot{m}_{31} = \dot{m}_{31}$	$\dot{E}_{des,TV2} = \dot{E}_{30} - \dot{E}_{31}$

integrated with the NSGA-II in MATLAB for optimization. The ANN model was trained on data generated from the EES simulations to establish accurate predictive correlations between design/operating parameters and performance indicators. The NSGA-II algorithm was then employed to solve the multi-objective optimization problem, balancing conflicting objectives.

The processes of simulations, analyses, and optimization conducted in this study are summarized in Fig. 2, which outlines the methodological workflow. Furthermore, the initial input design parameters used in the simulations are presented in Table 1, serving as the baseline for the research.

For system simulation, the following assumptions are applied [39,43]:

- Air is composed of 21% oxygen and 79% nitrogen.
- The system operates under steady-state conditions.
- All system components are considered adiabatic.
- Pressure losses within pipelines and exchangers are neglected.
- Throttling valves are assumed to function under constant enthalpy conditions.
- The outlet states of the evaporator and condenser are maintained at the saturated liquid and saturated vapor states.
- Compressors, turbines, and pumps are represented using adiabatic efficiency rather than ideal isentropic behavior.

3.1. Thermodynamic analysis

The thermodynamic analysis of the proposed system is based on the application of first and second laws of thermodynamics to each

Table 3
The data used for exergoeconomic assessment.

Parameter	Value
Lifetime	20 years
Operational time in the year	8760 h
Interest rate	12%
Maintenance factor	1.06
Unit cost of biogas	14.39 $/GJ

component and the overall cycle. The energy balance equations are applied to quantify the input and output energy streams, enabling the calculation of system energy efficiency. In parallel, the exergy balance equations are developed to evaluate the quality of energy conversion, identify irreversibilities, and determine exergy destruction. These balances form the foundation for calculating the overall energy and exergy efficiencies of the system, which serve as key indicators of its thermodynamic performance.

In line with the laws of mass and energy conservation, the following balance equations are considered for a control volume k operating under steady-state conditions [44]:

$$\sum \dot{m}_{in,k} = \sum \dot{m}_{out,k} \tag{1}$$

$$\dot{Q}_k - \dot{W}_k = \sum \dot{m}_{out,k} h_{out,k} - \sum \dot{m}_{in,k} h_{in,k} \tag{2}$$

where $\dot{m}$ denotes flow rate of mass, $\dot{Q}$ is rate of heat transfer, $\dot{W}$ is work, and h is specific enthalpy. Also, in and out show the input and output of the control volume.

For exergy analysis, the destruction rate of exergy in control volume k under steady-state operation can be expressed as [44]:

$$\dot{E}_{des,k} = \sum_j \left(1 - \frac{T_0}{T_{j,k}}\right) \dot{Q}_{j,k} - \dot{W}_k + \sum_i \dot{E}_{in,k} - \sum_i \dot{E}_{out,k} = \dot{E}_{F,k} - \dot{E}_{P,k} \tag{3}$$

or

$$\dot{E}_{des,k} = \dot{E}_{F,k} - \dot{E}_{P,k} \tag{4}$$

In eq. 3, $\sum_j \left(1 - \frac{T_0}{T_{j,k}}\right) \dot{Q}_{j,k}$ is the term showing the heat loss exergy rate, $\dot{W}_k$ is the work exergy rate, $\sum_i \dot{E}_{in,k}$ is the input streams' exergy rate, and $\sum_i \dot{E}_{out,k}$ is the output streams' exergy rate. Also, $\dot{E}_{F,k}$ denotes the fuel exergy rate and $\dot{E}_{P,k}$ presents the product exergy rate.

Table 2 summarizes the detailed mass, energy, and exergy balance equations applied to each system component.

Based on the proposed system illustrated in Fig. 1 and the performed thermodynamic study, the evaluation of the system's product capacities is presented. In this context, the electricity output ($\dot{W}_{net}$) and cooling output ($\dot{Q}_{Cooling}$) are determined using the following formulations [44]:

$$\dot{W}_{net} = \dot{W}_{GT} + \dot{W}_{SCT1} + \dot{W}_{SCT2} - \dot{W}_{AB} - \dot{W}_{SCC1} - \dot{W}_{SCC2} - \dot{W}_{pump1} - \dot{W}_{pump2} \tag{5}$$

$$\dot{Q}_{Cooling} = \dot{m}_{49} h_{49} - \dot{m}_{50} h_{50} \tag{6}$$

Subsequently, the total rate of exergy destruction is found by [44]:

$$\dot{E}_{des,tot} = \sum_{k=1}^{n} \dot{E}_{des,k} \tag{7}$$

Finally, the thermal and exergy efficiencies associated with the whole structure are defined as [39,40]:

$$\eta_{th} = \frac{\dot{W}_{net} + \dot{Q}_{Cooling}}{\dot{m}_{biogas}\, LHV_{biogas}} \times 100 \tag{8}$$

$$\eta_{ex} = \frac{\dot{W}_{net} + \left(\dot{E}_{49} - \dot{E}_{50}\right)}{\dot{E}_1} \times 100 \tag{9}$$

where $\dot{m}_{biogas}$ and LHV_{biogas} denote the biogas flow rate and the lower heating value of the biogas fuel.

1.1. Sustainability analysis

Following the thermodynamic and exergy analyses, the sustainability assessment evaluates the long-term feasibility of the system. This analysis aims to quantify how efficiently the system utilizes natural resources while minimizing ecological damage, thereby balancing immediate energy needs with sustainable practices. The sustainability performance is often expressed using a sustainability index (SI), which is defined as [45]:

$$SI_{tot} = \frac{1}{D_p} \tag{10}$$

where D_p is the depletion factor, formulated as [45]:

$$D_p = \frac{\dot{E}_{des,tot}}{\dot{E}_1} \tag{11}$$

A higher SI_{tot} value indicates a system that is more environmentally friendly and resource-efficient, reflecting its capacity to deliver energy services with reduced ecological impact.

3.2. Economic analysis

The exergoeconomic analysis provides a structured approach to evaluate the economic performance of energy systems by linking exergy flows to their associated costs. It quantifies the cost of heat losses, work, and material streams, enabling assessment of component-level and overall system financial viability. The general cost balance for a control volume k can be expressed as [46]:

$$\dot{C}_{\dot{Q}_k} + \sum \dot{C}_{in,k} + \dot{Z}_{k,PY} = \dot{C}_{\dot{W}_k} + \sum \dot{C}_{out,k} \tag{12}$$

where $\dot{Z}_{k,PY}$ is the updated investment cost for the present year (PY), $\dot{C}_{\dot{Q}_k}$ and $\dot{C}_{\dot{W}_k}$ represent heat loss cost rate and work cost rate, and $\sum \dot{C}_{in,k}$ and $\sum \dot{C}_{out,k}$ denote the costs of input and output streams.

The cost rate of any exergy stream can be defined as [46]:

$$\dot{C} = c\, \dot{E} \tag{13}$$

where c is denotes the unit cost of exergy.

The reference-year investment cost of the control volume k, $\dot{Z}_{k,RY}$, is determined from component purchase cost (Z), operational time (N), capital recovery factor (CRF), and maintenance factor (φ) [46]:

$$\dot{Z}_{k,RY} = Z_k \frac{CRF\, \varphi}{N} \tag{14}$$

with CRF calculated as:

$$CRF = \frac{i_r (1 + i_r)^n}{(1 + i_r)^n - 1} \tag{15}$$

where i_r is the annual interest rate and n is the system lifetime. Input parameters for the analysis, including system lifetime, operating hours, maintenance factor, fuel prices, and interest rate, are summarized in Table 3. Table 4 summarizes the cost balance, auxiliary cost, and investment cost equations applied to each component of the system.

The PY investment cost rate can be estimated using the chemical engineering plant cost index (CEPCI) [46]:

Table 4
Each component's cost balance, auxiliary cost, and investment cost equations.

Component	Cost balance equation	Investment cost equation	Auxiliary cost equation
Biogas combustion and GT section			
Air blower	$\dot{C}_1 + \dot{Z}_{AB} + \dot{C}_{W,AB} = \dot{C}_2$	$\dot{Z}_{AB} = \left(\frac{71.1 \times \dot{m}_1}{0.9 - \eta_{AB}}\right)\left(\frac{P_2}{P_1}\right)\ln\left(\frac{P_2}{P_1}\right)$	$c_{W,AB} = c_{W,GT\,1}; c_1 = 0$
Combustion chamber	$\dot{C}_2 + \dot{C}_7 + \dot{Z}_{CC} = \dot{C}_3$	$Z_{CC} = \left(\frac{48.64 \times \dot{m}_2}{0.995 - \left(\frac{P_3}{P_2}\right)}\right)(1 + \exp(0.018 \times T_3 - 26.4))$	$c_7 = 14.39\ \$/GJ$
Gas turbine	$\dot{C}_3 + \dot{Z}_{GT} = \dot{C}_4 + \dot{C}_{W,GT}$	$Z_{GT} = \left(\frac{1536 \times \dot{m}_3}{0.92 - \eta_{is,GT}}\right)\left(\frac{P_3}{P_4}\right)(1 + \exp(0.036 \times T_3 - 54.4))$	$c_3 = c_4$
MSC cycle			
Gas heater1	$\dot{C}_4 + \dot{C}_9 + \dot{Z}_{GH1} = \dot{C}_5 + \dot{C}_{27}$	$Z_{GH1} = 130 \times \left(\frac{A_{GH1}}{0.093}\right)^{0.78}$	$c_4 = c_5$
Gas heater2	$\dot{C}_5 + \dot{C}_{18} + \dot{Z}_{GH2} = \dot{C}_6 + \dot{C}_{19}$	$Z_{GH2} = 130 \times \left(\frac{A_{GH2}}{0.093}\right)^{0.78}$	$c_5 = c_6$
HTL	$\dot{C}_{10} + \dot{C}_{26} + \dot{Z}_{HTL} = \dot{C}_{11} + \dot{C}_{27}$	$Z_{HTL} = 130 \times \left(\frac{A_{HTL}}{0.093}\right)^{0.78}$	$c_{10} = c_{11}$
LTL	$\dot{C}_{11} + \dot{C}_{24} + \dot{Z}_{LTL} = \dot{C}_{25} + \dot{C}_{12}$	$Z_{LTL} = 130 \times \left(\frac{A_{LTL}}{0.093}\right)^{0.78}$	$c_{11} = c_{12}$
Heat exchanger1	$\dot{C}_{20} + \dot{C}_{17} + \dot{Z}_{HE1} = \dot{C}_{18} + \dot{C}_{21}$	$Z_{HE1} = 130 \times \left(\frac{A_{HE1}}{0.093}\right)^{0.78}$	$c_{20} = c_{21}$
Heat exchanger2	$\dot{C}_{16} + \dot{C}_{53} + \dot{Z}_{HE2} = \dot{C}_{54} + \dot{C}_{22}$	$Z_{HE2} = 130 \times \left(\frac{A_{HE2}}{0.093}\right)^{0.78}$	$c_{16} = c_{22}$
SCT1	$\dot{C}_9 + \dot{Z}_{SCT1} = \dot{C}_{10} + \dot{C}_{W,SCT1}$	$Z_{SCT1} = 479.34 \times \left(\frac{\dot{m}_9}{0.93 - \eta_{,SCT1}}\right)\ln\left(\frac{P_9}{P_{10}}\right) \times (1 + \exp(0.036 \times T_9 - 54.4))$	$c_9 = c_{10}$
SCT2	$\dot{C}_{19} + \dot{Z}_{SCT2} = \dot{C}_{20} + \dot{C}_{W,SCT2}$	$Z_{SCT2} = 479.34 \times \left(\frac{\dot{m}_{19}}{0.93 - \eta_{SCT2,}}\right)\ln\left(\frac{P_{19}}{P_{20}}\right) \times (1 + \exp(0.036 \times T_9 - 54.4))$	$c_{19} = c_{20}$
SCC1	$\dot{C}_{13} + \dot{Z}_{SCC1} + \dot{C}_{W,SCC1} = \dot{C}_{14}$	$Z_{SCC1} = \left(\frac{71.1 \times \dot{m}_{13}}{0.9 - \eta_{SCC1}}\right)\left(\frac{P_{14}}{P_{13}}\right)\ln\left(\frac{P_{14}}{P_{13}}\right)$	$c_{W,SCC1} = (\dot{C}_{W,SCT1} + \dot{C}_{W,SCT2})/(\dot{W}_{SCT1} + \dot{W}_{SCT2})$
SCC2	$\dot{C}_{22} + \dot{Z}_{SCC2} + \dot{C}_{W,SCC2} = \dot{C}_{23}$	$Z_{SCC2} = \left(\frac{71.1 \times \dot{m}_{22}}{0.9 - \eta_{SCC2}}\right)\left(\frac{P_{23}}{P_{22}}\right)\ln\left(\frac{P_{23}}{P_{23}}\right)$	$c_{W,SCC2} = (\dot{C}_{W,SCT1} + \dot{C}_{W,SCT2})/(\dot{W}_{SCT1} + \dot{W}_{SCT2})$
GAX cycle			
Absorber	$\dot{C}_{42} + \dot{C}_{29} + \dot{C}_{28} + \dot{C}_{52} = \dot{C}_{31} + \dot{C}_{44} + \dot{C}_{39} + \dot{C}_{51} + \dot{Z}_{abs}$	$Z_{abs} = 130\left(\frac{A_{abs}}{0.093}\right)^{0.78}$	$\left(\dot{C}_{39} + \dot{C}_{31}\right)/(\dot{E}_{39} + \dot{E}_{31}) = \dot{C}_{28}/\dot{E}_{28}$ $(\dot{C}_{44} + \dot{C}_{31})/(\dot{E}_{44} + \dot{E}_{31}) = \dot{C}_{29}/\dot{E}_{29}$ $\dot{C}_{29}/\dot{E}_{29} = \dot{C}_{42}/\dot{E}_{42}; c_{51} = 0$
GAXA	$\dot{C}_{42} + \dot{C}_{40L} = \dot{C}_{40V} + \dot{C}_{31} + \dot{Z}_{GAXA}$	$Z_{GAXA} = 130\left(\frac{A_{GAXA}}{0.093}\right)^{0.78}$	$\dot{C}_{40L} - \left(\dot{C}_{40V} + \dot{C}_{31}\right)/(\dot{E}_{40L} - \left(\dot{E}_{40V} + \dot{E}_{31}\right)) = (\dot{C}_{42} - \left(\dot{C}_{40V} + \dot{C}_{31}\right)/(\dot{E}_{42} - \left(\dot{E}_{40V} + \dot{E}_{31}\right))$
Generator	$\dot{C}_8 + \dot{C}_{30} + \dot{C}_{32} = \dot{C}_6 + \dot{C}_{33} + \dot{C}_{29} + \dot{C}_{43} + \dot{Z}_{gen}$	$Z_{gen} = 130\left(\frac{A_{gen}}{0.093}\right)^{0.78}$	$(\dot{C}_{32} - \dot{C}_{29})/(\dot{E}_{32} - \dot{E}_{29}) =$ $(\dot{C}_{30} - \dot{C}_{29})/(\dot{E}_{30} - \dot{E}_{29}); c_6 = c_8$
GAXD	$\dot{C}_{32} + \dot{C}_{41L} = \dot{C}_{41V} + \dot{C}_{33} + \dot{C}_{29} + \dot{C}_{43} + \dot{Z}_{GAXD}$	$Z_{GAXD} = 130\left(\frac{A_{GAXD}}{0.093}\right)^{0.78}$	$(\dot{C}_{41L} - \left(\dot{C}_{41V} + \dot{C}_{29} + \dot{C}_{33} + \dot{C}_{43}\right))/(\dot{E}_{41L} - \left(\dot{E}_{41V} + \dot{E}_{29} + \dot{E}_{33} + \dot{E}_{43}\right)) = (\dot{C}_{32} - \left(\dot{C}_{41V} + \dot{C}_{29} + \dot{C}_{33} + \dot{C}_{43}\right))/(\dot{E}_{32} - \left(\dot{E}_{41V} + \dot{E}_{29} + \dot{E}_{33} + \dot{E}_{43}\right))$
Heat exchanger3	$\dot{C}_{36} + \dot{C}_{39} = \dot{C}_{38} + \dot{C}_{35} + \dot{Z}_{HE3}$	$Z_{HE3} = 130\left(\frac{A_{HE3}}{0.093}\right)^{0.78}$	$c_{35} = c_{36}$
Condenser	$\dot{C}_{35} + \dot{C}_{48} = \dot{C}_{34} + \dot{C}_{47} + \dot{Z}_{cond}$	$Z_{cond} = 130\left(\frac{A_{cond}}{0.093}\right)^{0.78}$	$c_{34} = c_{35}; c_{47} = 0$
Evaporator	$\dot{C}_{38} + \dot{C}_{50} = \dot{C}_{37} + \dot{C}_{49} + \dot{Z}_{eva}$	$Z_{eva} = 130\left(\frac{A_{eva}}{0.093}\right)^{0.78}$	$c_{37} = c_{38}; c_{49} = 0$
Rectifier	$\dot{C}_{34} + \dot{C}_{33} + \dot{C}_{46} = \dot{C}_{32} + \dot{C}_{45} + \dot{Z}_{rect}$	$Z_{rect} = 130\left(\frac{A_{rect}}{0.093}\right)^{0.78}$	$c_{45} = c_{46}, c_{45} = 0$ $(\dot{C}_{34} - \dot{C}_{32})/(\dot{E}_{34} - \dot{E}_{32}) =$ $(\dot{C}_{33} - \dot{C}_{32})/(\dot{E}_{33} - \dot{E}x_{32})$
Pump1	$\dot{C}_{44} = \dot{C}_{28} + \dot{Z}_{pum1} + \dot{C}_{W,pum1}$	$Z_{pump1} = 3 \times 422 \times \dot{W}_{pump1}^{0.71} \times 1.41\{1 + (0.2/(1 - \eta_{is,pump1}))\}$	$c_{W,pump1} = (\dot{C}_{W,SCT1} + \dot{C}_{W,SCT2})/(\dot{W}_{SCT1} + \dot{W}_{SCT2})$
Pump2	$\dot{C}_{43} = \dot{C}_{42} + \dot{Z}_{pum2} + \dot{C}_{W,pum2}$	$Z_{pump2} = 3 \times 422 \times \dot{W}_{pump2}^{0.71} \times 1.41\{1 + (0.2/(1 - \eta_{is,pump2}))\}$	$c_{W,pump2} = (\dot{C}_{W,SCT1} + \dot{C}_{W,SCT2})/(\dot{W}_{SCT1} + \dot{W}_{SCT2})$
TV1	$\dot{C}_{37} = \dot{C}_{36} + \dot{Z}_{TV1}$	–	–
TV2	$\dot{C}_{31} = \dot{C}_{30} + \dot{Z}_{TV2}$	–	–

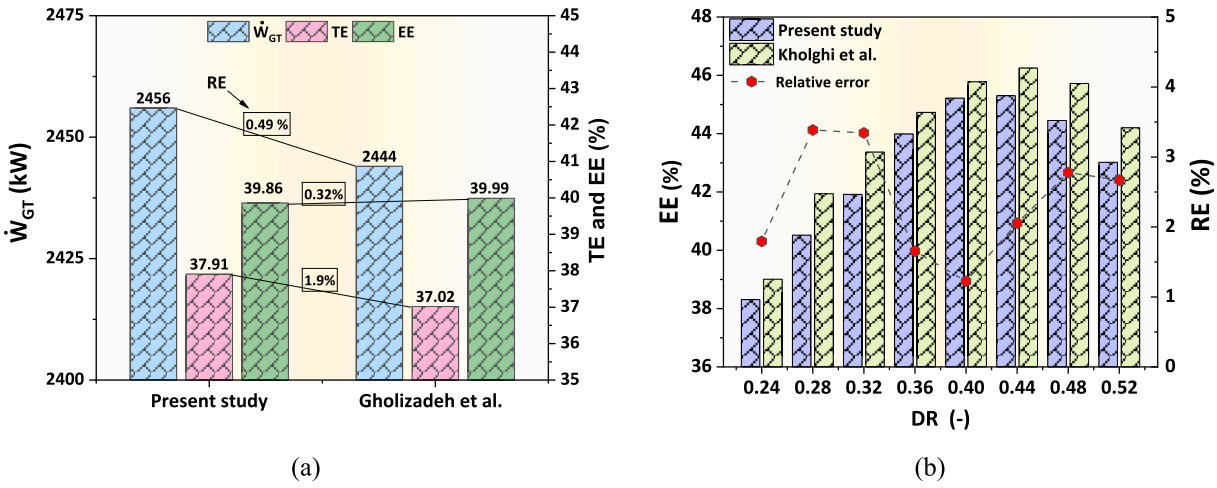

Fig. 3. Validation of the developed model: (a) biogas combustion-GT performance compared with Gholizadeh et al. [58]; (b) GAX cycle's exergy efficiency compared with Khoghi et al. [41].

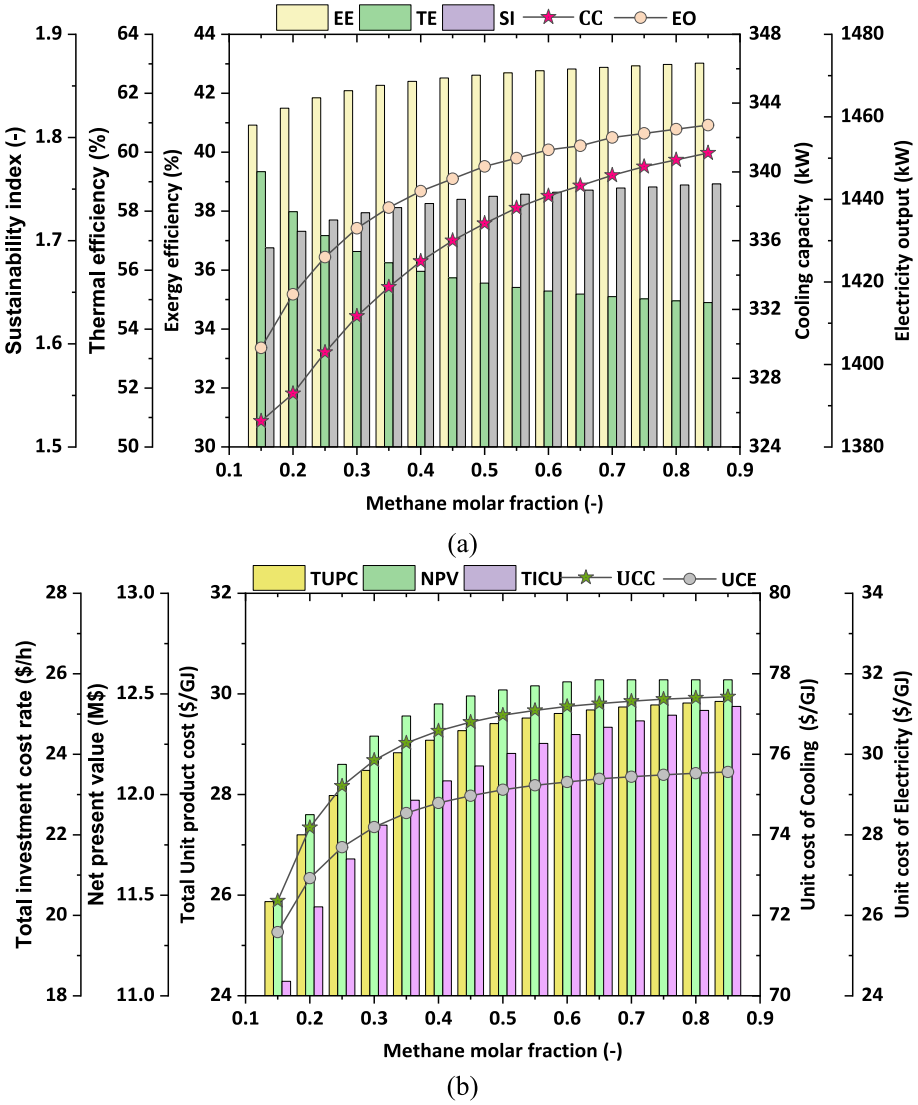

Fig. 4. Effect of methane molar fraction on the (a) thermodynamic-sustainability and (b) economic criteria.

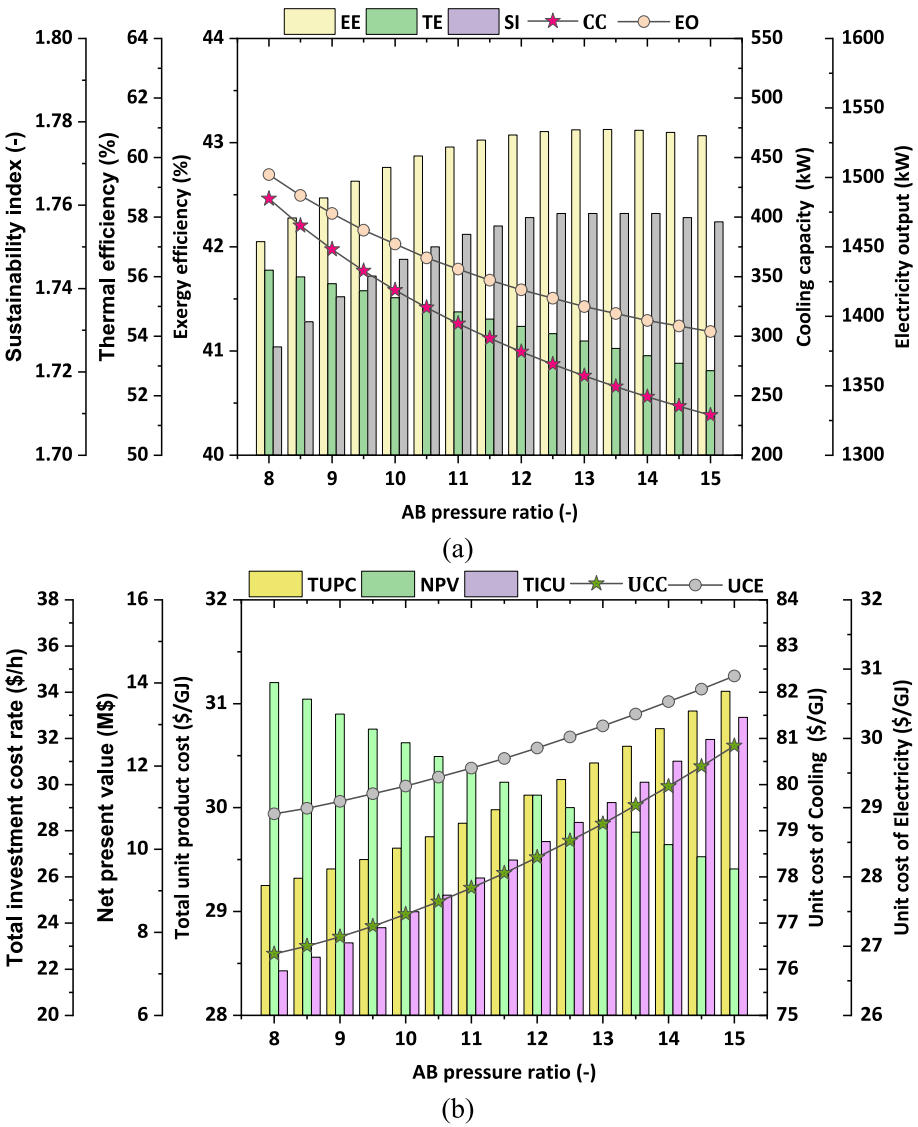

Fig. 5. Effect of AB pressure ratio on the (a) thermodynamic-sustainability and (b) economic criteria.

$$\dot{Z}_{k,PY} = \dot{Z}_{k,RY}\frac{CEPCI_{@PY}}{CEPCI_{@RY}} \tag{16}$$

Component-specific unit costs for fuel ($c_{F,k}$), product ($c_{P,k}$), and exergy destruction cost rate ($\dot{C}_{D,k}$) are calculated as [46]:

$$c_{F,k} = \frac{\dot{C}_{F,k}}{\dot{E}_{F,k}} \tag{17}$$

$$c_{P,k} = \frac{\dot{C}_{P,k}}{\dot{E}_{P,k}} \tag{18}$$

$$\dot{C}_{des,k} = c_{F,k}\dot{E}_{des,k} \tag{19}$$

The unit costs of electricity and cooling are calculated by [46]:

$$c_{elec} = \frac{\sum \dot{C}_{\dot{W}_{out,k}} - \sum \dot{C}_{\dot{W}_{in,k}}}{\dot{W}_{net}} = \frac{\dot{C}_{\dot{W}_{net}}}{\dot{W}_{net}} \tag{20}$$

$$c_{cooling} = \frac{\dot{C}_{50}}{\dot{E}_{50}} \tag{21}$$

Moreover, the total unit product cost (TUPC) for the overall system can be expressed as [46]:

$$TUPC = \frac{\dot{C}_{\dot{W}_{net}} + \dot{C}_{50}}{\dot{W}_{net} + \dot{E}_{50}} \tag{22}$$

Finally, the net present value (NPV) and payback period (PP) provide indicators of the system's economic feasibility [46]:

$$NPV = \left(\sum_{m=1}^{n} IF_m\ RDF_m\ AS\right) - FC \tag{23}$$

where FC is the fixed cost and AS is the annual savings. Other parameters include the inflation factor (IF) and the real discount rate (RDM) [46].

$$AS = AI - OC \tag{24}$$

$$OC = 0.06 \times FC \tag{25}$$

$$IF_m = \left(1 + \frac{R}{100}\right)^{-m} \tag{26}$$

$$RDF_m = \left(1 + \frac{RIR}{100}\right)^{-m} \tag{27}$$

In this context, the operating cost (OC) accounts for annual system

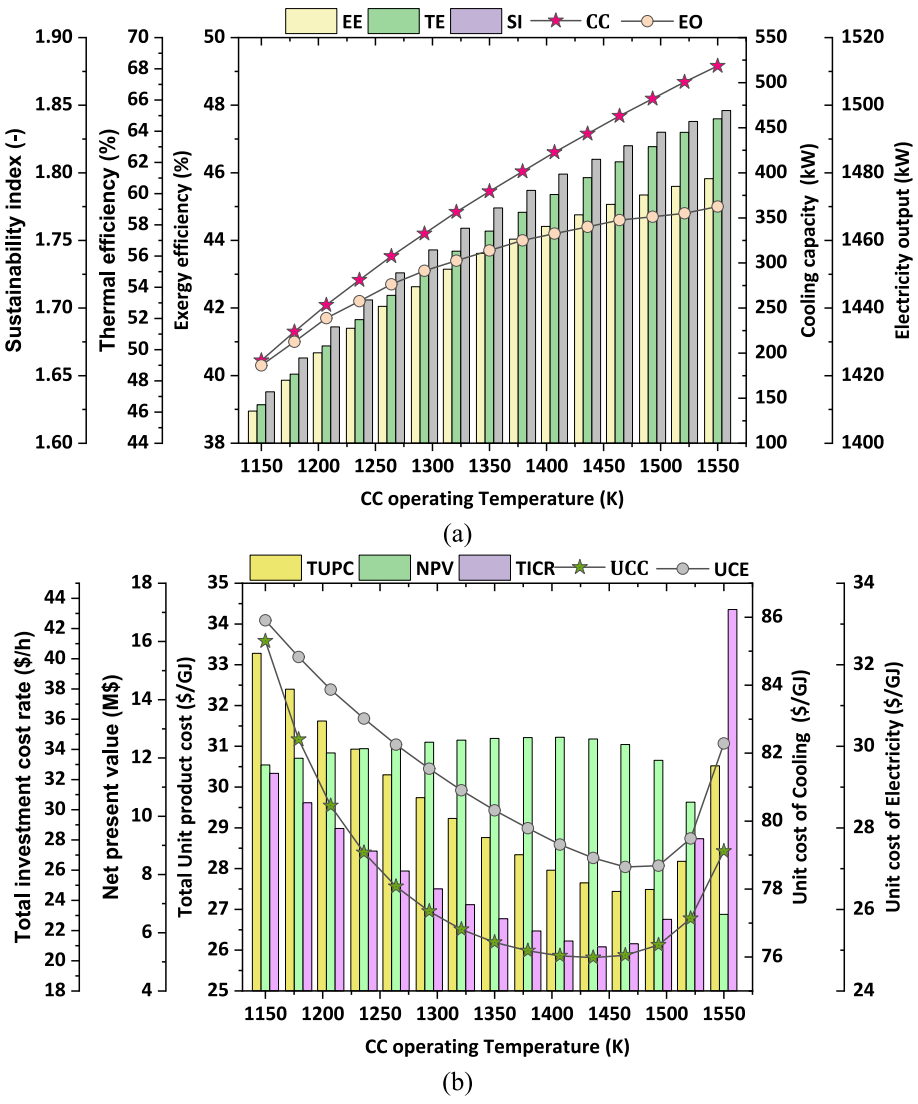

Fig. 6. Effect of CC operating temperature on the (a) thermodynamic-sustainability and (b) economic criteria.

expenses, while the annual income (AI) represents revenue generated. The variables R and RIR correspond to the inflation rate and the real interest rate, respectively. The payback period (PP) is determined as the time required for the NPV to become zero.

3.3. Environmental analysis

Evaluating the environmental aspect of the system is critical for understanding the impact of the planned biogas-fired systems. Such analysis provides essential data for compliance with environmental regulations and supports the development of cleaner and more sustainable energy systems [47]. In this study, the environmental impact of the system is evaluated by examining the emissions of NOx and CO, and the CO_2 emission rate. The emissions of NOx and CO can be estimated (in g pollutant per kg of fuel) as follows [48]:

$$m_{NOx} = \frac{0.15 \times 10^{16} \times \tau^{0.5} \times \exp\left(-71100/T_{pz}\right)}{P_2^{0.05} \times \left(\Delta P_{cc}/P_3\right)^{0.5}} \tag{28}$$

$$m_{CO} = \frac{0.179 \times 10^{9} \times \exp\left(7800/T_{pz}\right)}{P_2^{2} \times \tau \times \left(\Delta P_{cc}/P_2\right)^{0.5}} \tag{29}$$

The adiabatic flame temperature in the primary zone, T_{pz}, can be calculated using [48]:

$$T_{pz} = \kappa \omega^{\alpha} \exp\left[\beta(\omega+\lambda)^2\right] \Pi^{x^*} \Theta^{y^*} \Psi^{z^*} \tag{30}$$

$$x^* = a_1 + b_1\omega + c_1\omega^2 \tag{31}$$

$$y^* = a_2 + b_2\omega + c_2\omega^2 \tag{32}$$

$$z^* = a_3 + b_3\omega + c_3\omega^2 \tag{33}$$

Here, Π and Θ denote the dimensionless pressure (P_2/P_0) and dimensionless temperature (T_2/T_0), respectively. Ψ represents the H/C atomic ratio, and τ is the primary zone residence time (0.002 s).

Also, $\kappa, \alpha, \beta, \lambda, a_i, b_i, c_i$ are constants. The parameter ω depends on the fuel–air equivalence ratio ϕ as follows [48]:

$$\omega = \begin{cases} \phi; \phi < 1 \\ \phi - 0.7; \phi \geq 1 \end{cases} \tag{34}$$

$$\phi = \frac{(FA)_{actual}}{(FA)_{stoichiometric}} \tag{35}$$

where FA is the fuel to air ratio.

Finally, the CO_2 emission rate (CO_2ER) is determined as follows [34]:

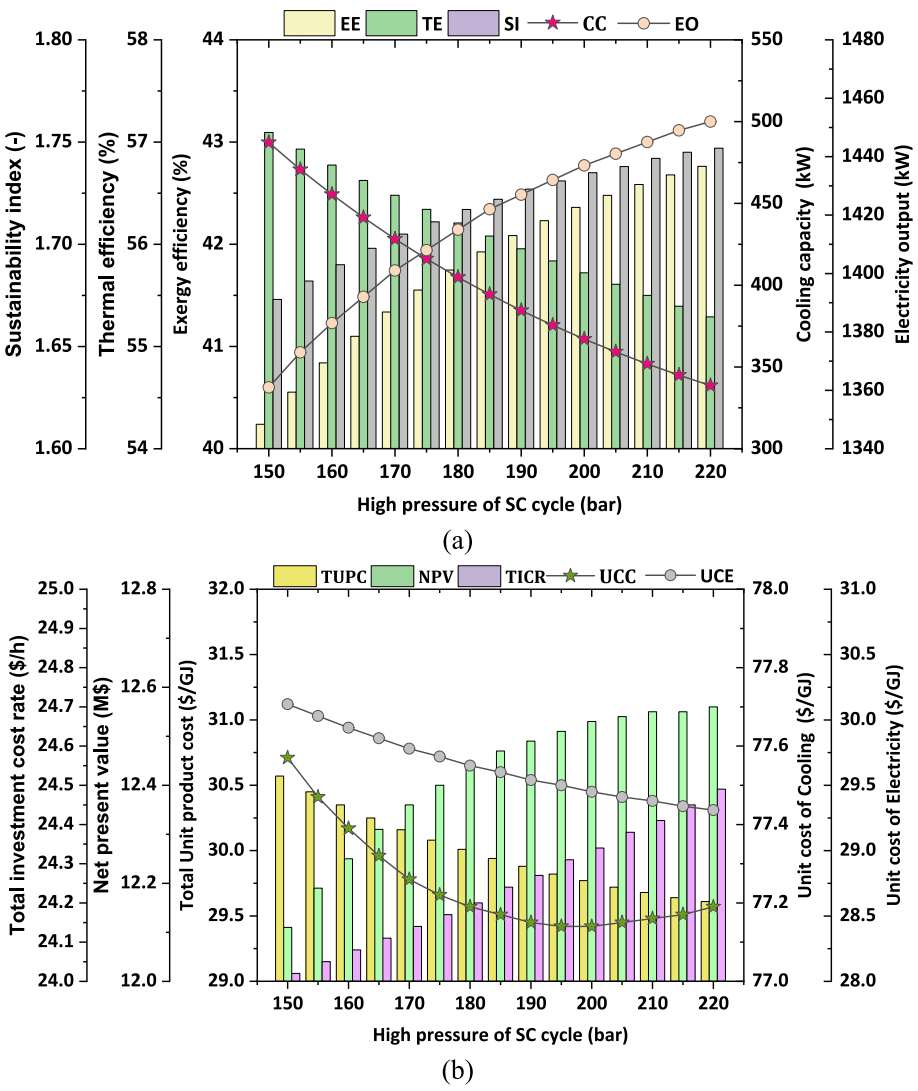

Fig. 7. Effect of high pressure of MSC cycle on the (a) thermodynamic-sustainability and (b) economic criteria.

$$CO_2ER = \frac{\dot{m}_{CO_2}}{\dot{W}_{net} + \dot{Q}_{Cooling}} \times 3600 \quad (36)$$

1.2. Optimization

Optimization plays a crucial role in engineering design, particularly in the development of energy systems, where efficiency, cost-effectiveness, and environmental performance must be balanced simultaneously [49,50]. Modern energy systems are inherently complex, integrating multiple subsystems with nonlinear interactions and conflicting goals. Without optimization, system design may lead to excessive energy losses, high operating costs, and significant environmental impacts. Moreover, optimization enables engineers to identify trade-offs among different objectives, improving decision-making and long-term sustainability [51,52]. In renewable and multi-generation systems, where performance depends on diverse factors such as fuel composition, thermodynamic parameters, and subsystem integration, optimization is indispensable. Thus, optimization serves as a bridge between theoretical modeling and practical application, enabling advanced energy systems to operate at their highest potential [53].

The optimization process in this study was structured as follows:

- Selection of objective functions.
- Identification of decision variables: Key thermodynamic and operating parameters defined within specified ranges.
- Data generation: 2000 samples produced using EES simulations.
- Data training: Development of intelligent models of objective functions via ANN.
- Optimization: Multi-objective optimization performed using NSGA-II.
- Decision-making: Final solution selected through the TOPSIS method.

The optimization framework is built upon three objective functions: sustainability index (SI), net present value (NPV), and total unit product cost (TUPC). The SI was chosen to reflect the environmental and resource-depletion impacts of the system, ensuring that solutions support long-term viability. The NPV was included to evaluate the economic profitability of the system across its lifetime, accounting for investment, operation, and revenue. Meanwhile, the TUPC measures the cost of producing system outputs (electricity, heating, and cooling), offering a benchmark for affordability and competitiveness.

The optimization process relies on selecting decision variables that have the greatest influence on system performance. In this study, five critical parameters were identified:

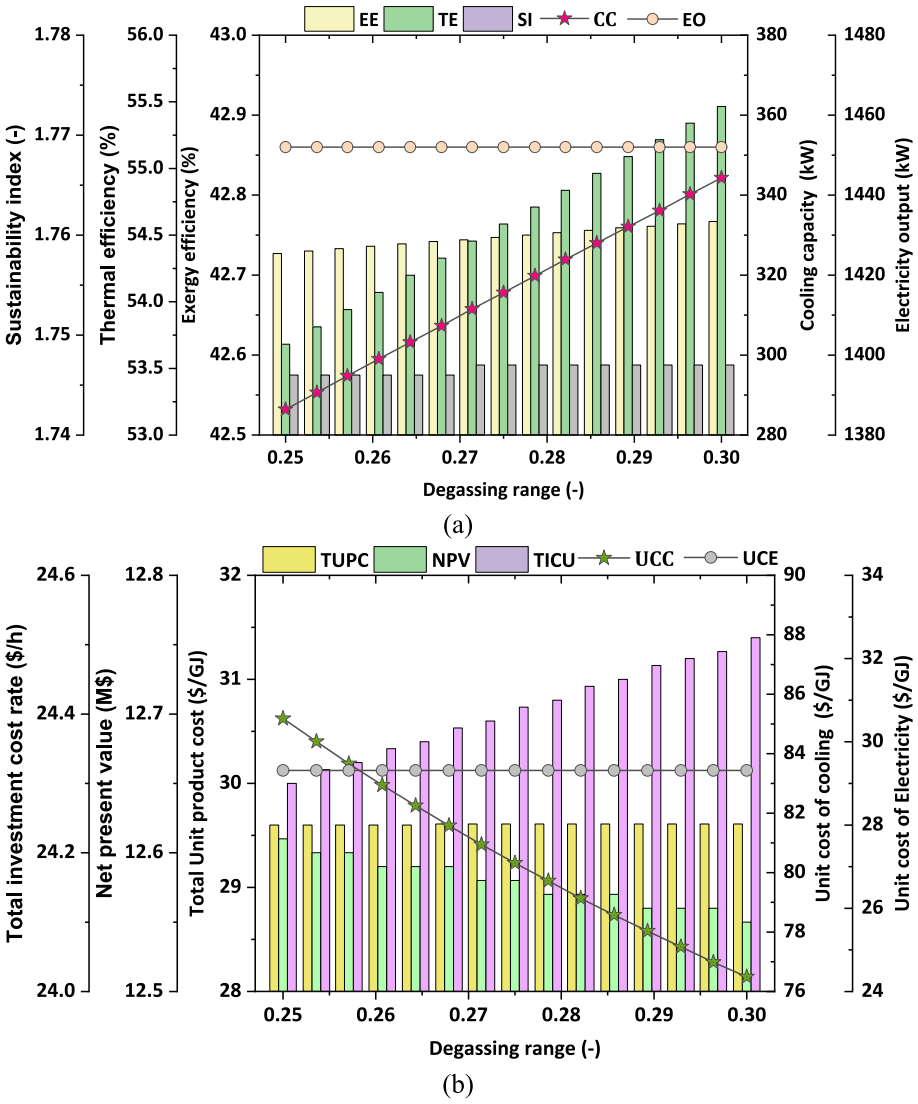

Fig. 8. Effect of degassing range on the (a) thermodynamic-sustainability and (b) economic criteria.

- Methane molar fraction (0.15–0.85): Since fuel composition strongly affects combustion efficiency and emissions, methane content was considered a key decision variable.
- Air blower pressure ratio (8–15): This variable governs the airflow and combustion characteristics.
- CC operating temperature (1150–1550 K): The flame temperature is directly linked to power output and efficiency.
- High pressure of MSC cycle (150–220 bar): This parameter determines the thermodynamic performance of the supercritical cycle.
- Degassing range (0.25–0.30): This range refers to the concentration difference between the strong and weak solutions in the GAX cycle.

By systematically varying the decision variables, the optimization explores a wide design space to achieve the best balance among efficiency, sustainability, and economic objectives. To support this process, EES was employed to generate a dataset of 2000 samples across the defined parameter ranges, ensuring comprehensive coverage of the multidimensional design space. Each sample provided corresponding values of the three objective functions (SI, NPV, TUPC), computed through thermodynamic, exergoeconomic, and sustainability analyses. This dataset forms the foundation for the subsequent machine-learning-based surrogate modeling.

To capture the nonlinear relations between the input decision variables and output objectives, an ANN-based ML process was defined based on the feedforward neural network architecture. Feedforward networks are particularly suitable for this type of problem because they can efficiently approximate complex mappings without requiring iterative physical simulations. The network architecture consisted of an input layer with five neurons corresponding to the decision variables and an output layer with three neurons representing the objective functions. The hidden layers included two fully connected layers, each with 12 neurons, employing the sigmoid activation function, which was chosen for its ability to model nonlinear interactions effectively. The network is trained using the Marquardt–Levenberg algorithm [54], selected for its fast convergence and robust error minimization capabilities.

To ensure reliable generalization, the dataset was split into 70% for training, 15% for validation, and 15% for testing. The training set was used to adjust network weights, the validation set guided hyperparameter tuning and prevented overfitting, and the test set assessed the predictive performance of the trained ANN [55]. These surrogate models significantly reduced computational cost and enabled efficient application of the NSGA-II algorithm in the optimization stage.

The multi-objective optimization problem was solved using the NSGA-II method [56]. This method is widely recognized for its robustness, elitism preservation, and ability to handle conflicting objectives

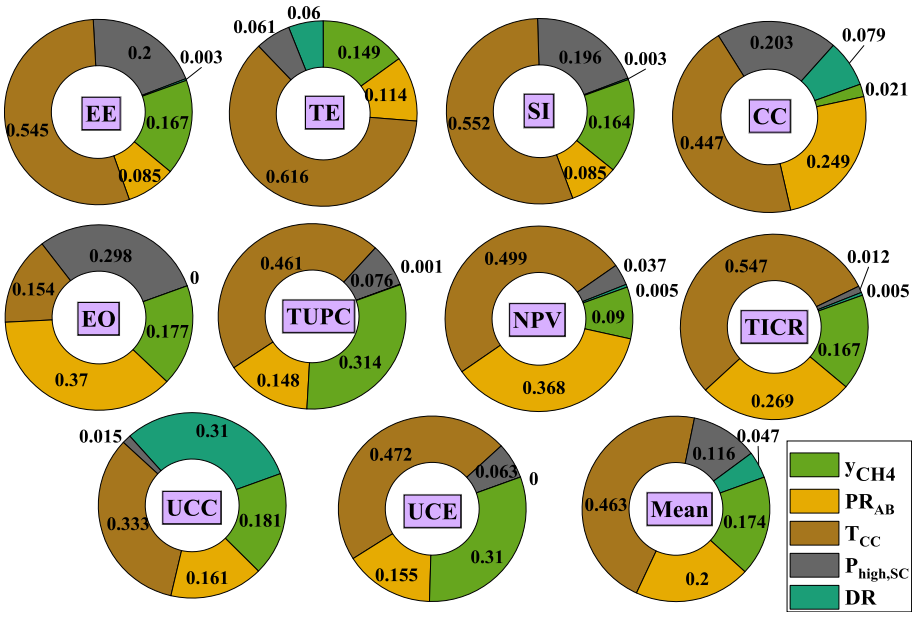

Fig. 9. Sensitivity analyses results derived from the parametric study.

simultaneously. The algorithm begins with a randomly generated initial population, with each individual representing a possible combination of decision variables. Through iterative operations—selection, crossover, and mutation—new generations are produced. The fitness of individuals is evaluated using the ANN-based surrogate models of the objective functions. NSGA-II employs a fast non-dominated sorting approach to classify individuals into Pareto fronts and a crowding distance measure to maintain diversity within the solution set. Over successive generations, the algorithm converges toward the Pareto-optimal front, representing trade-off solutions among SI, NPV, and TUPC.

After obtaining the Pareto-optimal set from NSGA-II, the Technique for Order Preference by Similarity to Ideal Solution (TOPSIS) method [57] was applied for decision-making. TOPSIS identifies the best compromise solution by measuring each alternative's relative closeness to the ideal solution (maximum SI and NPV, minimum TUPC) and the negative-ideal solution. The method ranks all Pareto-optimal solutions based on this relative closeness, ultimately selecting the one that offers the most balanced performance across all objectives.

4. Results and discussions

This section presents the findings of the study, combining simulation, thermodynamic and economic analyses, and optimization to evaluate the performance of the proposed multigeneration system. The discussion is divided into three main parts, presented in the following.

4.1. Validation

This subsection presents the validation results in this study. By comparing simulation outcomes with well-established literature results, the validation process verifies that the adopted assumptions, governing equations, and numerical methods accurately represent real-world behavior. Fig. 3 illustrates the validation results for the biogas combustion-GT section and GAX cycle.

Based on Fig. 3a, the performance of the biogas combustion-GT section was validated by comparing the predicted production capacity, thermal efficiency, and exergy efficiency with the results reported by Gholizadeh et al. [58]. The comparison shows a maximum relative error of only 1.9%, indicating that the present model accurately captures the thermodynamic behavior of the GT subsystem. This small margin of error confirms the reliability of the adopted assumptions and governing equations for representing biogas-based GT performance.

Similarly, Fig. 3b validates the GAX cycle, where exergy efficiency was evaluated across a degassing range between 0.24 and 0.52. The simulation results were compared against the reference data provided by Khoghi et al. [41], showing a maximum relative error of 3.3%. This close agreement highlights the robustness of the developed model in predicting the performance of the GAX subsystem under varying operating conditions.

4.2. Parametric analysis

The methane molar fraction in biogas plays a pivotal role in shaping both the thermodynamic and economic performance of the system (Fig. 4). Increasing the methane content from 0.15 to 0.85 enhances the fuel quality, which strengthens combustion characteristics and reduces internal irreversibility. As a result, the system delivers higher useful outputs, with power production increasing from 1404 kW to 1458 kW and cooling capacity rising from 325.5 kW to 341.1 kW. Although the improved LHV augments energy production, it has a stronger impact on the input side of the thermal efficiency calculation, leading to a decline in thermal efficiency from 59.34% to 54.89%. In contrast, exergy-based indicators reveal a net thermodynamic advantage. The exergy rate of the useful outputs grows more rapidly than the input exergy, yielding an increase in exergy efficiency from 40.92% to 43.02%. This improvement reflects a more effective utilization of the available energy potential. Similarly, the SI rises from 1.693 to 1.755, indicating a more favorable balance between useful exergy production and exergy destruction as methane concentration increases. From an economic perspective (Fig. 4b), methane enrichment introduces a clear trade-off between performance gains and cost escalation. The total investment cost rate increases from 18.36 $/h to 25.19 $/h due to the requirement for higher-capacity and higher-performance components. This, combined with increased exergy flow rates in system streams, drives the TUPC upward from 25.87 $/GJ to 29.85 $/GJ. Correspondingly, the unit cost of cooling rises from 72.36 $/GJ to 77.43 $/GJ, while the unit cost of electricity increases from 25.58 $/GJ to 29.56 $/GJ. Despite these higher costs, the system produces greater quantities of electricity and cooling per unit of fuel input, which enhances overall productivity. This improvement offsets part of the cost increase and contributes to a higher NPV, strengthening the project's financial viability and long-term attractiveness.

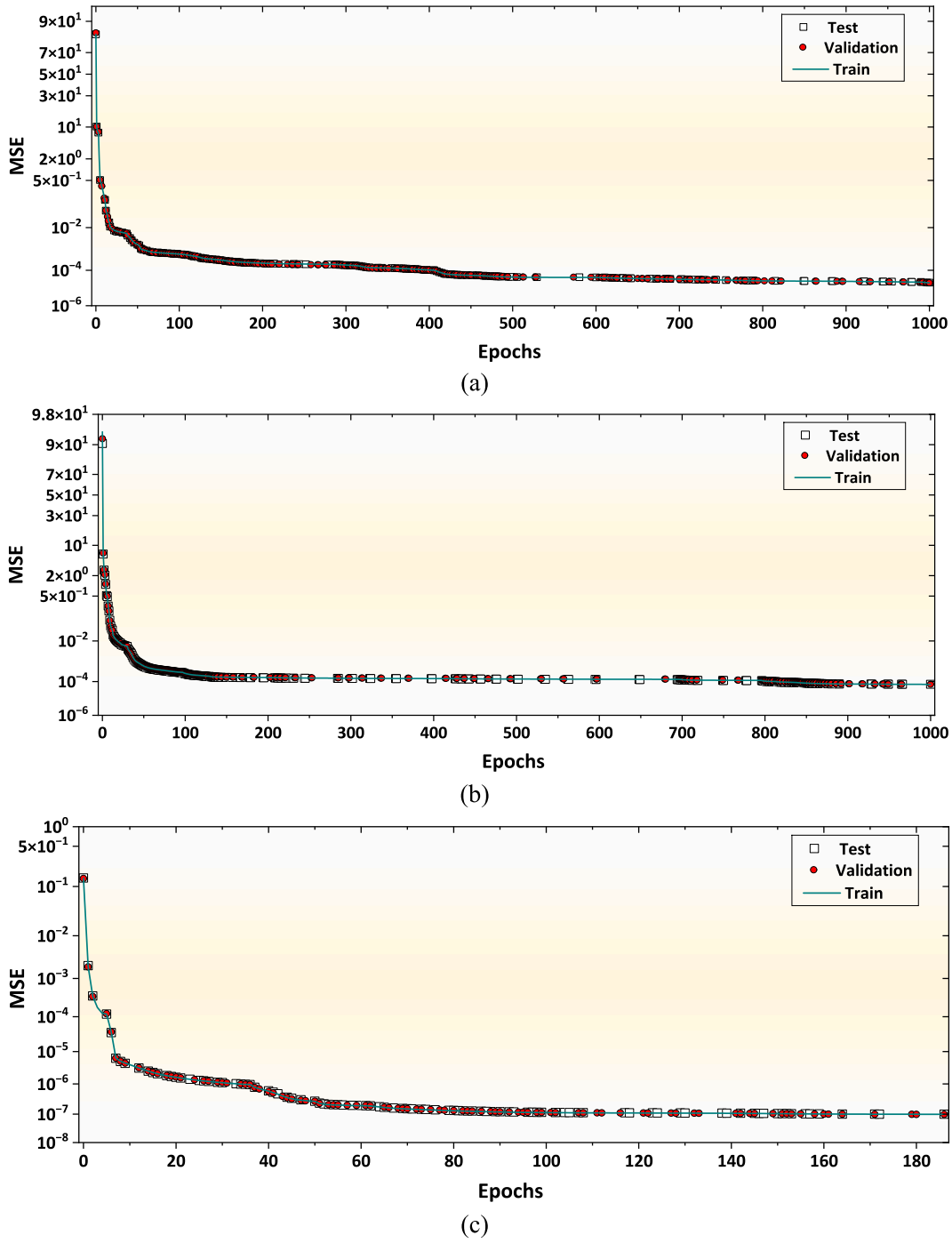

Fig. 10. Validation of the ANN convergence based on mean squared error (MSE) for (a) TUPC, (b) NPV, and (c) SI.

Varying the AB pressure ratio exerts a marked influence on both thermodynamic-sustainability and economic performance (Fig. 5). Increasing the pressure ratio from 8 to 15 intensifies the compression work requirement, which progressively offsets the gains in power generation and leads to a reduction in overall system productivity. As a result, electricity output decreases from 1502 kW to 1389 kW, while cooling capacity experiences a more substantial decline, from 415.4 kW to 233.6 kW. This loss of useful outputs directly translates into a reduction in thermal efficiency from 56.2% to 52.8%, indicating a less favorable conversion of fuel energy into net products at higher pressure ratios. Exergy-based indicators, however, reveal a more nuanced behavior. Exergy efficiency increases slightly from 42.05% to a maximum of 43.13% at a pressure ratio of 13.5, accompanied by a rise in the SI from 1.726 to 1.758 at the same operating point. This initial improvement is primarily attributed to the reduction in required biogas flow rate at higher pressure ratios, which lowers the input exergy rate. Beyond a pressure ratio of approximately 13, the continued decline in electricity and cooling outputs becomes dominant, causing both exergy efficiency and SI to decrease marginally despite further increases in pressure ratio. From an economic standpoint (Fig. 5b), increasing the AB pressure ratio leads to higher costs and diminished financial performance. The total investment cost rate rises from 21.9 $/h to 32.9 $/h due to the need for more robust and expensive compression equipment. Simultaneously, the TUPC increases from 29.25 $/GJ to 31.12 $/GJ, reflecting both elevated capital costs and reduced useful energy production. The unit cost of cooling increases from 76.3 $/GJ to 80.8 $/GJ,

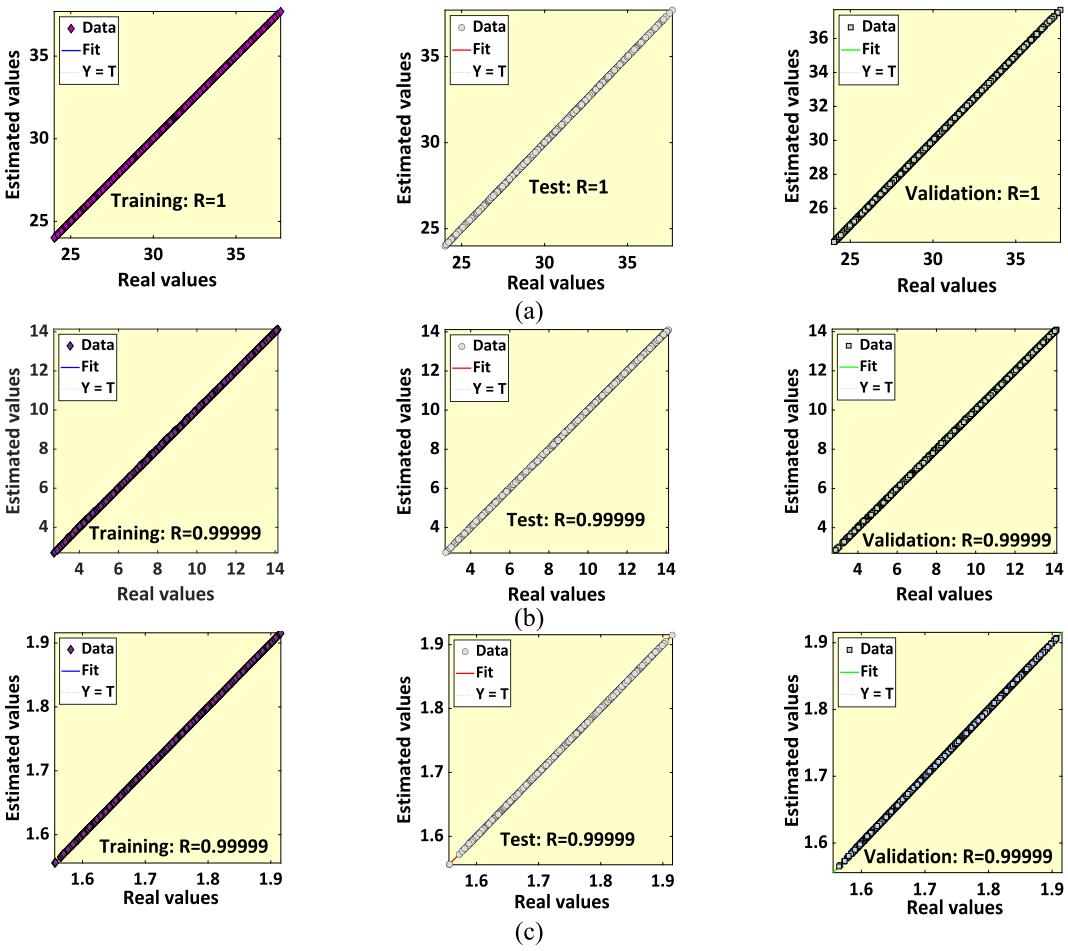

Fig. 11. Validation of the ANN based on regression coefficient for (a) TUPC, (b) NPV, and (c) SI.

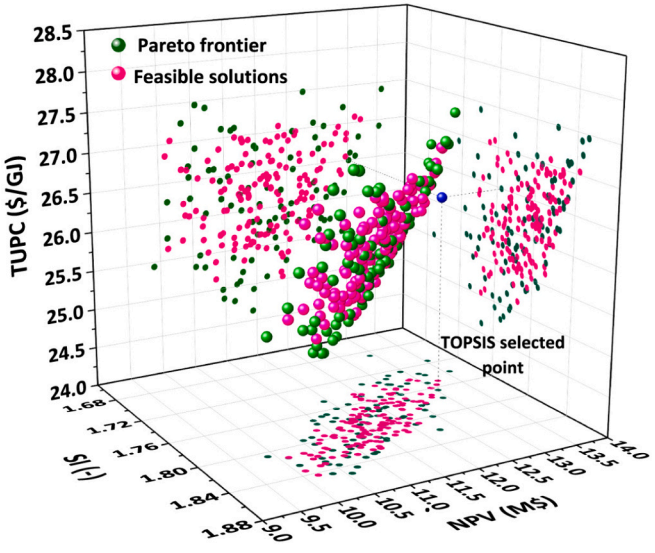

Fig. 12. Pareto front generated by the NSGA-II method.

while the unit cost of electricity rises from 28.9 $/GJ to 30.9 $/GJ, making the delivered energy services less competitive. Consequently, the NPV declines from 14.01 M$ to 9.52 M$, indicating lower profitability and a longer payback period at higher pressure ratios.

Varying the CC temperature has a pronounced impact on the thermodynamic–sustainability and economic behavior of the system (Fig. 6).

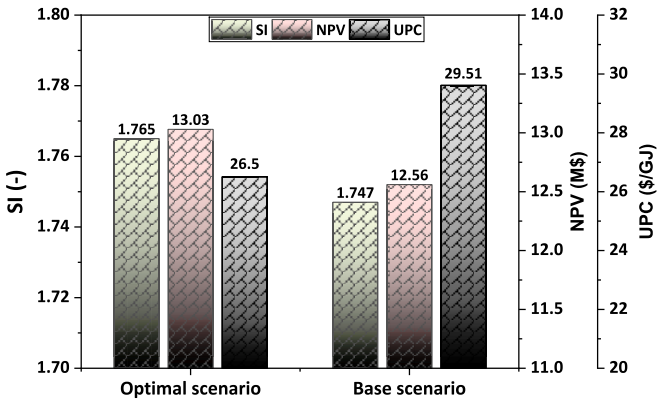

Fig. 13. Optimum results derived from the Pareto front diagram.

Increasing the CC temperature enhances the chemical-to-thermal energy conversion per unit mass of biogas, resulting in higher flame temperatures and exhaust gases with greater specific enthalpy. This raises the turbine inlet temperature and increases the work extracted by the gas turbine and downstream cycles, thereby strengthening overall system performance. As the CC temperature increases from 1150 K to 1550 K (Fig. 6a), useful energy outputs rise, although with different sensitivities. Electricity production increases moderately from 1423 kW to 1470 kW, whereas cooling capacity exhibits a much stronger response, increasing from 191.8 kW to 518.6 kW. These gains in product capacities lead to a marked improvement in thermodynamic performance. Thermal efficiency increases steadily from 46.46% to 64.80%, reflecting more effective utilization of the fuel's energy content. At the same time, exergy efficiency improves from 38.95% to 45.83%, indicating a reduction in internal irreversibility and a higher quality of energy conversion at elevated combustion temperatures. The SI also increases monotonically, from 1.638 to 1.846, confirming that higher CC temperatures favor a more sustainable operating regime. The economic response to CC temperature variation (Fig. 6b) exhibits a clear optimum rather than a monotonic trend. As CC temperature rises, improved output capacities initially dominate, causing the TUPC to decrease from 33.28 $/GJ at 1150 K to a minimum of 27.44 $/GJ at 1464 K. Consistently, the unit cost of electricity decreases from 33.09 $/GJ to 27.04 $/GJ at 1464 K, while the unit cost of cooling declines from 85.3 $/GJ to 75.98 $/GJ at 1436 K. Beyond these temperatures, further increases in CC temperature lead to higher capital and operating costs, reversing the trend and raising TUPC to 30.52 $/GJ, the unit cost of cooling to 79.11 $/GJ, and the unit cost of electricity to 30.07 $/GJ at 1550 K. This trade-off is also reflected in the investment and profitability indicators. The total investment cost rate decreases from 32.41 $/h at 1150 K to a minimum of 20.92 $/h at 1436 K, before increasing sharply to 43.26 $/h at 1550 K. Correspondingly, the NPV rises from 11.76 M$ to a maximum of 12.71 M$ at 1407 K, driven by improved thermodynamic performance and lower unit product costs. At higher CC temperatures, however, escalating costs outweigh the thermodynamic benefits, causing the NPV to decline significantly to 6.63 M$ at 1550 K.

Increasing the high pressure of the MSC cycle from 150 bar to 220 bar substantially reshapes the distribution of useful outputs and, consequently, the thermodynamic and economic behavior of the system (Fig. 7). Higher MSC pressure enhances heat recovery and raises the turbine inlet enthalpy within the MSC cycle, which strengthens electricity generation and increases the system's net power output from 1361 kW to 1452 kW. This improvement, however, is achieved at the expense of cooling production, as a greater fraction of the recovered heat is diverted away from the GAX cycle. As a result, cooling capacity declines sharply from 487.2 kW to 338.6 kW, revealing a clear trade-off between maximizing electricity generation and maintaining cooling output. This redistribution of useful products explains the contrasting efficiency trends. Exergy efficiency improves steadily from 40.24% to 42.76%, reflecting the growing dominance of net electricity production, which has a higher exergy content. In contrast, thermal efficiency decreases from 57.09% to 55.29%, primarily due to the pronounced reduction in cooling output. The SI increases with pressure, indicating that higher MSC pressures favor long-term operational robustness despite the loss in cooling capacity. The corresponding economic indicators (Fig. 7b) suggest a modest improvement in overall attractiveness. The TUPC decreases from 30.57 $/GJ to 29.61 $/GJ, while the NPV increases from 12.11 M$ to 12.56 M$, driven mainly by the higher-value electricity output. At the product level, the unit cost of electricity decreases from 30.12 $/GJ to 29.31 $/GJ, whereas the unit cost of cooling increases slightly from 77.57 $/GJ to 77.19 $/GJ, reflecting the reduced cooling production.

Fig. 8 illustrates the effect of varying the degassing range in the GAX cycle from 0.25 to 0.30. Increasing the degassing range strengthens desorption, which enhances refrigerant circulation to the evaporator and leads to a noticeable increase in cooling output from 286.4 kW to 344.3 kW. This improvement directly supports a rise in thermal efficiency from 53.68% to 55.47%, indicating more effective utilization of the recovered heat for cooling production. Exergy efficiency also increases slightly, from 42.73% to 42.77%, suggesting marginal gains in energy utilization with negligible additional irreversibility. The sustainability index remains nearly unchanged, varying only between 1.746 and 1.747, which implies that the thermodynamic benefits of increasing the degassing range have a limited impact on long-term sustainability. From an economic standpoint (Fig. 8b), variations in the degassing range primarily affect cooling-related metrics, as electricity production remains constant at 1452 kW. Consequently, the TUPC remains nearly unchanged at approximately 29.6 $/GJ, and the NPV stays close to 12.6 M$, indicating minimal influence on overall profitability. A significant benefit is observed in the unit cost of cooling, which decreases from 85.18 $/GJ to 76.49 $/GJ due to the higher cooling output distributing fixed costs over a larger useful product. In contrast, the unit cost of electricity remains constant at 29.31 $/GJ, consistent with the unchanged power generation level.

Fig. 9 presents the sensitivity analysis derived from the parametric study (Figs. 4–8), highlighting the relative importance of each decision variable on the system's thermodynamic, sustainability, and economic performance. Among the parameters, the combustion chamber temperature emerges as the most influential factor, with the highest sensitivity index across nearly all criteria, except for net electricity output where its effect is less dominant. On average, CC temperature records a mean sensitivity index of 0.463, underscoring its critical role in driving productivity, efficiency, and sustainability outcomes. This strong influence is attributed to its direct effect on combustion intensity, turbine inlet conditions, and the quality of energy conversion. The AB pressure ratio is identified as the second most impactful parameter, with a mean sensitivity index of 0.200. Its significance lies in how compression work and system pressure levels affect both power generation and irreversibilities, thereby influencing thermal and exergy efficiencies. Following this, the methane molar fraction of the biogas fuel ranks third, with an average sensitivity index of 0.174. Variations in fuel composition directly modify the LHV, which alters the balance between electricity, cooling production, and efficiency metrics. The high pressure of the MSC cycle exhibits a moderate influence, with a mean sensitivity index of 0.116, primarily due to its impact on heat recovery and the trade-off between cooling and power production. Finally, the degassing range of the GAX cycle demonstrates the lowest sensitivity, with a mean index of just 0.047, confirming that while degassing range influences cooling performance, its effect on overall system performance and economic viability is relatively minor compared to other decision variables.

4.3. Optimization results

This section presents the outcomes of the optimization process,

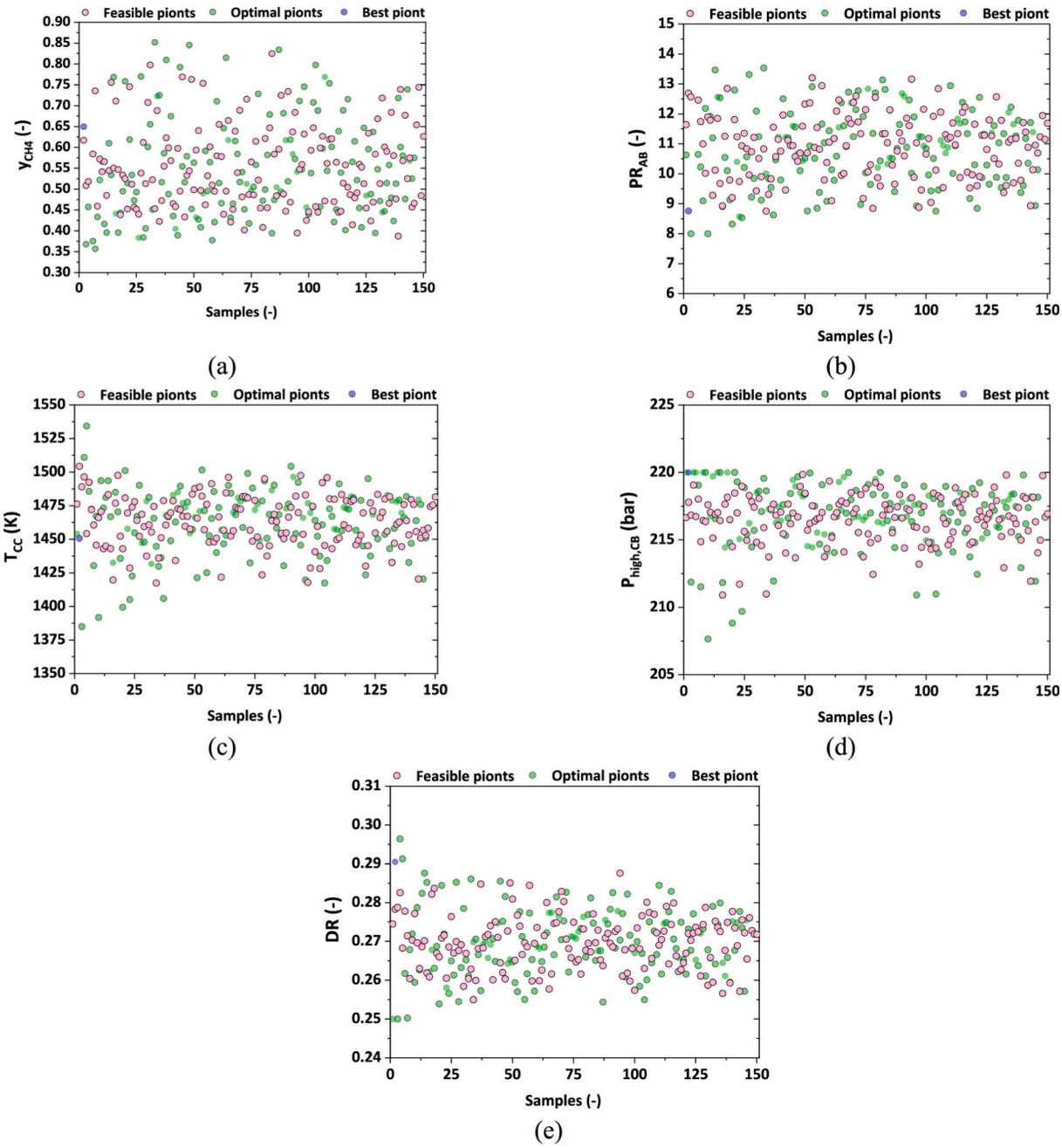

Fig. 14. Scatter distribution of decision variables.

combining ANN-based modeling with the NSGA-II algorithm and decision-making via TOPSIS. First, the accuracy and predictive capability of the ANN model are discussed. Then, the Pareto frontier is analyzed to illustrate trade-offs between objectives. Finally, the optimized case is selected and evaluated against baseline performance.

4.3.1. ANN results

Fig. 10 illustrates the convergence behavior of the ANN during training, expressed in terms of the mean squared error (MSE) for the three selected objective functions: TUPC, NPV, and SI. The ANN demonstrates excellent convergence, with the MSE values for TUPC and NPV remaining below 10^{-5}, while the MSE for SI is below 10^{-7}. These low error levels indicate that the ANN effectively captures the nonlinear relations between the decision variables and the objective functions. The stable and smooth decline in MSE confirms that the training process is free from overfitting or underfitting, ensuring reliable predictive performance for optimization purposes.

Fig. 11 validates the ANN's accuracy using the regression coefficient (R) between predicted and actual data for the training, testing, and validation sets. The results show regression coefficients equal to 1 for TUPC and 0.999 for NPV and SI, signifying an almost perfect correlation between ANN predictions and the original EES-generated data. This high degree of accuracy highlights the ANN's capability to model complex thermodynamic and exergoeconomic behaviors with minimal deviation. Furthermore, the consistency across training, testing, and validation subsets confirms the robustness and generalization capability of the ANN, making it a reliable surrogate model for the subsequent optimization using the NSGA-II algorithm.

4.3.2. Pareto frontier

Fig. 12 presents the Pareto front diagram obtained for the multi-objective optimization by NSGA-II method, highlighting the trade-offs

between the three conflicting objectives, including TUPC, NPV, and SI. The results demonstrate that no single solution simultaneously maximizes or minimizes all objectives, which is expected in multi-objective optimization problems involving economic and sustainability indices. Instead, the Pareto front diagram provides a spectrum of optimal solutions, where improvement in one objective generally comes at the expense of another. To aid in the final selection, the TOPSIS decision-making method is applied to rank the Pareto solutions based on their relative closeness to the ideal point. Fig. 13 illustrates the final decision point selected using the TOPSIS method from the Pareto front diagram. At this optimal solution, the TUPC, NPV, and SI are found to be 26.5 $/GJ, 13.03 M$, and 1.765, respectively. Compared to the base mode, TUPC decreases by 10.2%, indicating a substantial reduction in production costs, while NPV and SI increase by 3.7% and 1.1%, respectively, highlighting improved economic profitability and sustainability. These results confirm the effectiveness of the NSGA-II and TOPSIS framework in achieving a well-balanced solution.

Fig. 14 illustrates the scatter distribution of decision variables within the optimization process, highlighting the regions where the most significant activities and feasible solutions are concentrated. As shown in Fig. 14a, the methane molar fraction exhibits the widest distribution, ranging primarily between 0.45 and 0.70, indicating that this range is particularly influential for achieving favorable objective outcomes. In Fig. 14b, the AB pressure ratio shows the greatest activity between 0.09 and 0.13, suggesting that a moderate pressure ratio is optimal for maintaining system efficiency while avoiding excessive compression work. Fig. 14c reveals that the CC operating temperature concentrates between 1425 and 1500 K, which balances effective combustion with

Table 5
Thermodynamic and economic properties of system's streams obtained for the optimum point.

State	T(K)	P(kPa)	$\dot{h}\left(\frac{kg}{kJ}\right)$	$s\left(\frac{kg}{kJ\ K}\right)$	$\dot{m}\left(\frac{kg}{s}\right)$	$\dot{E}$ (kW)	$c\ \left(\frac{\$}{kWh}\right)$	$\dot{C}\left(\frac{\$}{h}\right)$
1	293.2	101.3	−262.8	6.977	2.227	0	0	0
2	578.8	887.4	36.5	7.054	2.227	616.5	0.09827	60.58
3	1451	851.9	−1224	8.456	2.689	3113	0.07682	239.1
4	985.5	105.8	−1844	8.557	2.689	1366	0.07682	104.9
5	784.5	103.7	−2095	8.278	2.689	909.9	0.07682	69.9
6	559.2	101.6	−2363	7.882	2.689	502	0.07682	38.56
7	293.2	1200	−7657	8.967	0.462	3441	0.0518	178.3
8	394.9	99.55	−2549	7.495	2.689	307.6	0.07682	23.63
9	955.5	20,706	693.8	1.82E-01	2.795	1792	0.105	188.2
10	821.4	7400	536.3	2.03E-01	2.795	1334	0.105	140.1
11	565.7	7252	239.3	−2.25E-01	2.795	854.5	0.105	89.75
12	415.2	7107	70.37	−0.5691	2.795	664	0.105	69.74
13	415.2	7107	70.37	−0.5691	0.4752	112.9	0.105	11.86
14	539.3	21,560	174.6	−0.5398	0.4752	158.3	0.1105	17.49
15	415.2	7107	70.37	−0.5691	2.32	551.1	0.105	57.89
16	428.2	7104	85.37	−0.5334	4.944	1197	0.1056	126.5
17	390.7	22,000	−52.55	−1.042	2.624	664.5	0.1095	72.79
18	534.2	21,560	168.1	−0.5519	2.624	866.6	0.1168	101.2
19	754.5	21,129	442.5	−0.1175	2.624	1252	0.106	132.8
20	636.5	7400	319.3	−0.09583	2.624	912.5	0.106	96.77
21	439.8	7104	98.64	−0.5029	2.624	646.6	0.106	68.57
22	309.1	7400	−99.61	−1.06	4.944	1046	0.1056	110.5
23	390.7	22,000	−52.55	−1.042	4.944	1252	0.1095	137.1
24	390.7	22,000	−52.55	−1.042	2.32	587.6	0.1095	64.36
25	521	21,560	151	−0.5843	2.32	748.6	0.1131	84.69
26	524.1	21,560	155	−0.5766	2.795	906.8	0.1127	102.2
27	762.2	21,129	452	−0.1051	2.795	1350	0.1132	152.9
28	313.5	478.4	−59.21	0.4435	1.142	10,841	0.08527	924.4
29	358.4	1591	147	1.054	1.142	10,872	0.08528	927.2
30	423.2	1591	519.3	1.881	0.8518	3345	0.08498	284.3
31	384.9	478.4	519.3	1.911	0.8518	3338	0.08517	284.3
32	358.4	1591	1444	4.607	0.4352	8489	0.08524	723.6
33	358.4	1591	147	1.054	0.009726	92.55	0.09163	8.481
34	341.1	1591	1383	4.433	0.4255	8390	0.08525	715.2
35	314.2	1591	192.3	0.6779	0.4255	8351	0.08525	711.9
36	285.5	1560	54.38	0.218	0.4255	8350	0.08525	711.8
37	276.2	478.4	54.38	0.226	0.4255	8349	0.08526	711.8
38	278.2	478.4	1198	4.343	0.4255	8322	0.08526	709.5
39	304.2	468.9	1336	4.831	0.4255	8320	0.08531	709.8
40 L	358.4	478.4	199.5	1.116	0.7916	26.41	0.08847	2.336
40 V	358.4	478.4	1572	5.48	0.07463	2.729	0.08847	0.2414
41 L	384.9	1591	283.7	1.4	1.085	95.38	0.07537	7.189
41 V	384.9	1591	1565	4.923	0.233	73.88	0.07537	5.569
42	358.4	478.4	199.5	1.116	0.1348	669.9	0.08528	57.13
43	358.8	1591	202.1	1.119	0.1348	670.1	0.08539	57.22
44	313.9	1591	−56.49	0.4478	1.142	10,843	0.08531	925
45	293.2	101.3	83.93	0.2962	0.9178	0	0	0
46	303.2	101.3	125.8	0.4365	0.9178	0.6403	0	0
47	293.2	101.3	83.93	0.2962	12.11	0	0	0
48	303.2	101.3	125.8	0.4365	12.11	8.45	0.4322	3.652
49	293.2	101.3	83.93	0.2962	7.781	0	0	0
50	278.2	101.3	21.39	0.07722	7.781	12.84	0.2718	3.49
51	293.2	101.3	83.93	0.2962	10.62	0	0	0
52	303.2	101.3	125.8	0.4365	10.62	7.408	1.431	10.6
53	293.2	101.3	83.93	0.2962	10.93	0	0	0
54	313.2	101.3	167.6	0.5722	10.93	29.85	0.5483	16.37

Table 6
Exergy and exergoeconomic results of system's components obtained for the optimum point.

Element	$\dot{E}_F^k$(kW)	$\dot{E}_P^k$(kW)	$\dot{E}_{des}^k$(kW)	$\dot{C}_F^k$ ($/h)	$\dot{C}_P^k$ ($/h)	$\dot{C}_{des}^k$ ($/h)	$\dot{Z}^k$ ($/h)
AB	666.6	616.5	50.10	56.45	60.58	4.923	4.129
CC	4058	3113	945.30	238.80	239.1	72.62	0.2612
GT	1746	1667	79.92	134.20	141.1	6.768	6.977
GH1	456.1	441.2	14.88	35.04	35.32	1.191	0.2811
GH2	408	385.9	22.11	31.34	31.62	1.812	0.2829
HTR	479	443.6	35.40	50.31	50.68	4.044	0.3668
LTR	190.5	161	29.54	20.01	20.33	3.731	0.3216
HE1	265.9	202	63.90	28.20	28.41	8.985	0.2069
HE2	151.2	29.85	121.30	15.97	16.37	66.53	0.3938
SCT1	458.1	440.5	17.62	48.11	49.22	1.969	1.103
SCT2	340	323.3	16.70	36.05	37.11	1.917	1.056
SCC1	49.54	45.46	4.09	5.60	5.636	0.5066	0.03641
SCC2	232.7	206.4	26.30	26.30	26.66	3.398	0.3645
Generator				14.93	15.03	8.063	0.09637
Absorber	194.4	89.4	105	227.20	10.6	122.7	0.2479
TV1	8350	8349	1.00	711.80	711.8	0.08543	0.002045
TV2	3345	3338	7.43	284.30	284.3	0.6313	0.004094
Pump 1	3.103	1.653	1.45	0.35	0.5835	0.1639	0.2327
Pump 2	0.3479	0.2057	0.14	0.04	0.08854	0.01607	0.04921
Rectifier	6.638	0.6403	6.00	723.60	723.7	653.8	0.03254
Condenser	38.33	8.45	29.88	3.27	3.652	2.547	0.3847
HE3	1.327	2.174	3.50	0.11	0.296	0.2984	0.1829
Evaporator	26.95	12.84	14.11	2.30	3.49	1.203	1.192

Table 7
Comparison of results obtained for the optimized case and base mode.

Parameter	Base mode	Optimized case
Methane molar fraction, y_{CH4}(−)	0.60	0.65
Air blower pressure ratio, PR_{AB}(−)	10	8.76
Combustion chamber operating temperature, T_{CC}(K)	1300	1450
Supercritical CO_2 cycle high pressure, $P_{high,SC}$(bar)	220	220
Degassing range, DR (−)	0.295	0.2905
Net electricity output, $\dot{W}_{net}$(kW)	1452	1478
Cooling capacity, $\dot{Q}_{CC}$(kW)	338.6	486.6
Total thermal efficiency, TE_{tot}(%)	55.29	62.75
Total exergy efficiency, EE_{tot}(%)	42.76	43.32
Total exergy fuel rate, $\dot{E}_{F,tot}$(kW)	3415	3441
Total exergy product rate, $\dot{E}_{P,tot}$(kW)	1461	1491
Total exergy destruction rate, $\dot{E}_{des,tot}$(kW)	1721	1596
Total exergy loss rate, $\dot{E}_{L,tot}$(kW)	234	354.8
Sustainability index, SI(−)	1.747	1.765
Investment cost rate, $\dot{Z}_{tot}$($/h)	24.49	18.21
Total unit product cost, TUPC ($/GJ)	29.51	26.5
Unit cost of cooling ($/GJ)	77.19	75.5
Unit cost of electricity ($/GJ)	29.61	26.4
Exergoeconomic factor, f_{tot}($/h)	15.37	11.74
Net present value, NPV (M$)	12.56	13.03
Payback period, PP (year)	4.913	3.79

material and thermodynamic constraints. Fig. 14d demonstrates that the high-pressure level of the MSC cycle is most active within the 215–220 bar range, indicating that elevated pressure enhances cycle efficiency and supports higher exergy utilization. Lastly, Fig. 14e shows the degassing range clustering between 0.25 and 0.29, which reflects the critical role of solution concentration differences in stabilizing the GAX cycle performance.

4.3.3. Optimized case

Table 5 summarizes the thermodynamic and economic properties of the system's streams at the optimum operating point, including temperature, pressure, enthalpy, entropy, mass flow rate, exergy, and cost parameters. The results highlight how different sections of the system contribute to overall energy conversion and cost distribution. High-temperature and high-pressure streams (e.g., states 9–14, 17–27) carry significant exergy values, reflecting their critical role in power generation and refrigeration cycles. For instance, state 27 reaches 1350 kW exergy, underlining the effective utilization of high-pressure combustion products in driving the MSC cycle. Similarly, cooling-related streams (28–39) demonstrate very high exergy rates (over 8000 kW), emphasizing their strong contribution to system efficiency and product diversification. On the economic side, the cost rate ($\dot{C}$) distribution shows that the largest expenses are associated with streams that manage high exergy flows (e.g., 28, 29, 34–38), reaching values above 700 $/h, which reflects the intensive energy exchange occurring in these states.

Table 6 presents the exergy and exergoeconomic performance of system components at the optimum operating condition, highlighting the distribution of fuel exergy, product exergy, destructed exergy, and associated costs. The results reveal that the CC and HE2 are the most exergy-intensive components, with destruction rates of 945.3 kW and 121.3 kW, respectively. The rectifier and CC also exhibit the highest exergy destruction cost at 653.8 $/h and 72.6 $/h, respectively. Similarly, heat exchangers (HE1 and HE2) show notable exergy destruction (63.9 kW and 121.3 kW), with HE2 being particularly critical due to its high cost of destruction (66.5 $/h). In contrast, components such as pumps and valves TV1 and TV2 demonstrate very low exergy destruction (<2 kW) and minimal cost impact, confirming their limited role in system irreversibilities. The exergoeconomic results also highlight the absorber and generator, which show moderate exergy destruction (105 kW for the generator) but significant costs (over 120 $/h for the absorber). Also, the highest investment cost rates belong to the AB and CC at 6.977 $/h and 4.129 $/h, respectively.

Table 7 compares the base mode and optimized case, illustrating how the optimization framework enhances both thermodynamic and economic performance. From the design perspective, the methane molar fraction is slightly increased (0.60 → 0.65), while the AB pressure ratio decreases (10 → 8.76), and the CC temperature rises substantially (1300 → 1450 K). These shifts highlight a balance between improving combustion quality and reducing compression work. Thermodynamically, the total thermal efficiency improves significantly from 55.29% to 62.75%, while the exergy efficiency shows a smaller gain (42.76% → 43.32%). The increase in CC temperature enhances useful product exergy (1491 kW), while exergy destruction decreases by ~7.3% (1721 → 1596 kW). Indeed, the cooling capacity nearly increases by 44% (338.6 → 486.6 kW), confirming the system's improved polygeneration potential. Economically, optimization substantially reduces the investment cost rate (24.49 → 18.21 $/h) and the TUPC (29.51 → 26.5 $/GJ).

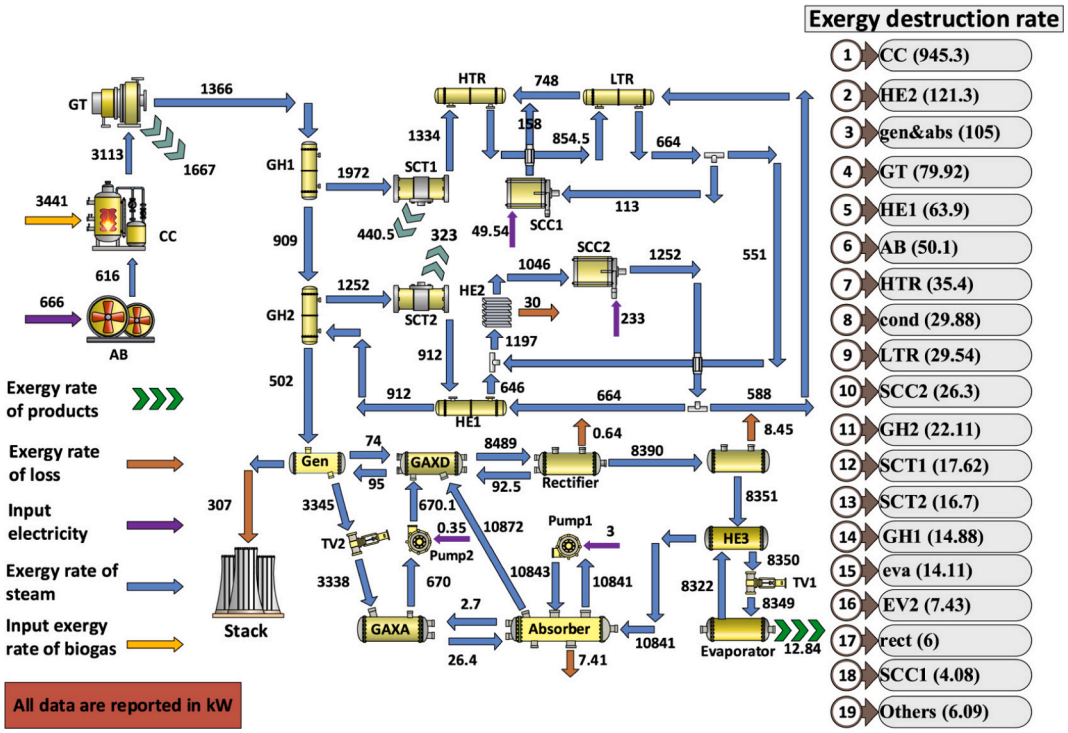

Fig. 15. Exergy flow diagram of the system under the optimized case.

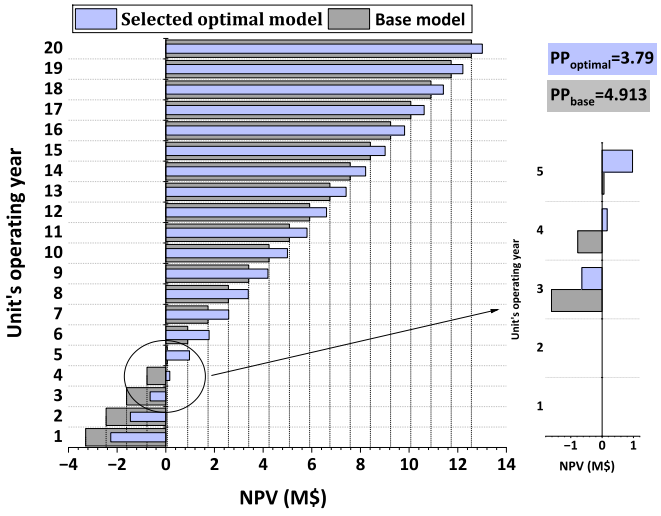

Fig. 16. The NPV during the operating year for both base mode and optimized case.

The unit cost of electricity declines by ~10% (29.61 → 26.4 $/GJ), while the unit cost of cooling shows a minor reduction (77.19 → 75.5 $/GJ). The exergoeconomic factor drops, indicating better alignment between thermodynamic and cost performance. Sustainability-wise, the sustainability index improves slightly (1.747 → 1.765), while the NPV increases from 12.56 M$ to 13.03 M$, and the payback period shortens notably (4.913 → 3.79 years). This confirms the optimized configuration delivers faster economic returns with enhanced efficiency. Thus, the optimized case achieves higher efficiency, lower costs, improved profitability, and greater cooling output, validating the effectiveness of the applied optimization strategy.

Fig. 15 illustrates the exergy flow diagram of the optimized system, highlighting the distribution of input exergy, useful outputs, and exergy destruction across all components. The exergy flow diagram emphasizes the system's strong performance in converting high-grade exergy into multiple useful outputs, while also identifying critical components responsible for the majority of exergy destruction, guiding future design improvements and operational strategies. The diagram provides a clear visual representation of where energy quality is most effectively utilized and where irreversibilities occur. From the plot, the CC clearly stands out as the largest source of exergy destruction, consistent with the high-temperature reactions and associated thermodynamic irreversibilities observed in Table 6. Other significant contributors include the high-temperature heat exchangers (HE1 and HE2) and turbomachinery (GT), indicating that thermal gradients and mechanical work conversion are key areas for potential efficiency improvement.

Fig. 16 presents the NPV and payback period trends for both the optimized and base modes of the system over a 20-year operational lifetime. The results demonstrate a clear economic advantage of the optimized configuration. In the optimized case, the NPV consistently remains higher than the base mode, reaching 13.03 M$, compared to 12.56 M$ for the base configuration. This increase reflects the combined effects of improved exergy performance and cost distribution, which translate into greater long-term revenue and cost savings. The payback period is also significantly reduced for the optimized system, falling to 3.79 years, compared to 4.91 years for the base mode. This shorter payback period indicates that the initial investment is recovered more quickly, highlighting the financial feasibility and attractiveness of the optimization strategy.

Fig. 17 illustrates the influence of fuel cost and interest rate on the NPV, PP, and TUPC of the optimized biogas-based system. As shown in Fig. 17a, increasing fuel cost leads to a decline in the NPV and a corresponding increase in both PP and TUPC, reflecting the direct impact of higher operating expenses on long-term profitability and product cost. In contrast, lower fuel costs enhance economic attractiveness by improving cash flow, shortening the PP, and reducing the TUPC. Fig. 17b demonstrates that the interest rate has a strong inverse effect on NPV, as higher discount rates reduce the present value of future revenues. Consequently, PP increases and TUPC rises with increasing interest rate, indicating greater financial burden and reduced investment appeal.

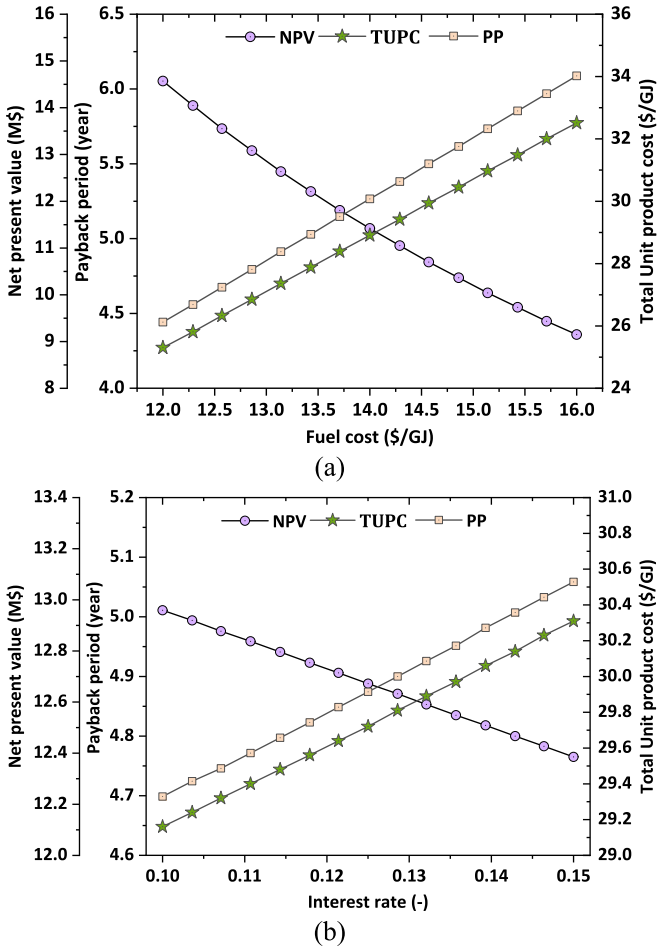

Fig. 17. Effect of (a) fuel cost and (b) interest rate on the NPV, PP, and TUPC under the optimized case.

These trends highlight the economic sensitivity of the proposed system to market-driven parameters and emphasize the importance of fuel price stability and favorable financing conditions for achieving robust economic performance under the optimized operating regime.

Fig. 18 compares the emissions of Nox and CO, and CO_2ER between the base and optimized scenarios of the proposed biogas-driven system. The optimized scenario demonstrates a notable reduction in CO emissions from 0.00194 g/kg fuel to 0.00151 g/kg fuel, indicating more complete combustion due to improved air–fuel mixing and operational conditions. Also, NOx emissions increase slightly from 5.512×10^{-9} g/kg fuel to 6.2×10^{-9} g/kg fuel, which can be attributed to elevated flame temperatures in the optimized configuration that favor NOx formation. In addition, CO_2ER increase from 0.5984 kg/kWh in the base scenario to 1.048 kg/kWh in the optimized scenario, reflecting higher fuel utilization in the optimized case. However, the environmental impact is favorable, with low NOx and CO emissions per kilogram of input fuel.

Table 8
Comparative performance assessment of the proposed biogas-based system with recent studies.

Reference	Fuel	Products	Main results
Ref. [14]	Biogas	Electricity	η_{en} = 37.25% η_{ex} = 21.27% TUPC = 21.46 $/GJ
Ref. [17]	Biogas	Electricity, cooling, and heating	η_{en} = 61.0% η_{ex} = 30.44% TUPC = 0.017 $/kWh PP = 6.11 years
Ref. [18]	Biogas and liquefied natural gas	Electricity and cooling	η_{en} = 80.79% η_{ex} = 41.5% TUPC = 9.81 $/GJ
Ref. [20]	Biogas	Electricity, cooling, and freshwater	η_{ex} = 49.32% TUPC = 27.54 $/GJ NPV = 18.32 M $ PP = 2.015 years
Ref. [21]	Biogas	Electricity and methanol	η_{en} = 43.63% η_{ex} = 46.52% TUPC = 28.36 $/GJ NPV = 160.0 M $ PP = 4.77 years
This study	Biogas	Electricity and cooling	η_{en} = 62.75% η_{ex} = 43.32% TUPC = 26.5 $/GJ NPV = 130.03 M$ PP = 3.76 years

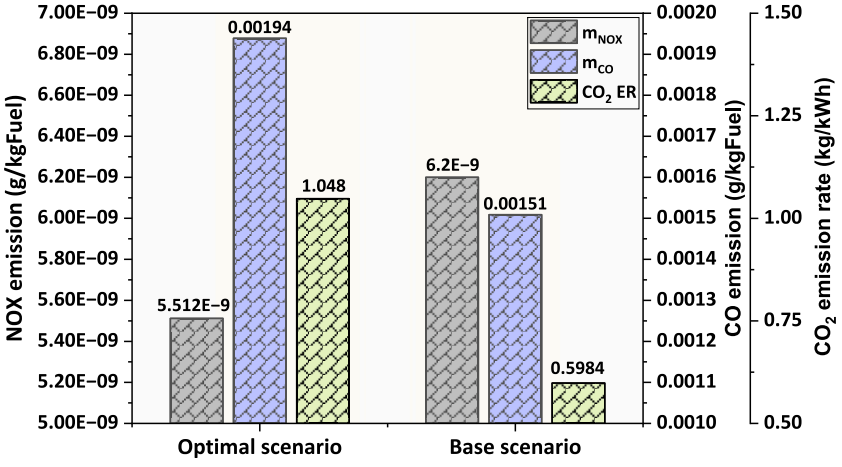

Fig. 18. Environmental analysis results under for both optimized and base scenarios.

4.4. Practical limitations and comparison with previous studies

While the present study demonstrates the thermodynamic, exergoeconomic, and sustainability potential of the proposed biogas-driven system, practical implementation may encounter several challenges. First, biogas quality and composition can vary depending on feedstock type, seasonal availability, and digester performance. Variations in methane content, moisture, or the presence of contaminants can affect combustion stability, turbine operation, and overall system efficiency. Addressing these issues requires robust fuel conditioning and real-time monitoring. Second, maintenance and operational considerations are critical. GT, MSC heat exchangers, and GAX refrigeration unit necessitate periodic inspection, cleaning, and replacement of consumables. These requirements can increase operational costs and impact long-term reliability. Advanced control strategies, predictive maintenance, and operator training are essential to ensure stable performance. Third, system integration and operational complexity present further practical hurdles. Coordinating the GT, MSC, and GAX cycles during start-up, shutdown, and transient operation requires precise control to prevent thermal fatigue and ensure safety. Implementing adaptive control systems, modular designs, and real-time monitoring can mitigate these challenges, while pilot-scale testing and gradual deployment are recommended to validate system performance under real-world conditions.

Table 8 presents a comparative evaluation of the proposed biogas-based system against recent studies reported in the literature. The comparison highlights the competitive thermodynamic efficiency and economic indicators achieved by the present configuration, particularly due to the integration of advanced thermodynamic cycles and a hybrid optimization framework. Differences observed among studies can be attributed to variations in system configuration, operating conditions, and optimization strategies.

5. Conclusions

This study investigated the thermodynamic, economic, and environmental performance of a novel hybrid energy system integrating a biogas combustion–GT unit, a MSC cycle, and a GAX cooling cycle, using a comprehensive methodology that combined parametric analysis, sensitivity analysis, ANN modeling, and multi-objective optimization (NSGA-II coupled with TOPSIS). The analysis quantified the effects of key design variables, including methane molar fraction, AB pressure ratio, CC temperature, MSC cycle high pressure, and GAX degassing range, while ANN modeling enabled accurate performance prediction across the design space, and the optimization framework produced Pareto-optimal solutions that balance efficiency, sustainability, and economic feasibility. The study's novel contributions include the simultaneous utilization of high- and low-grade thermal energy, the integration of advanced MSC and GAX cycles for enhanced system performance, and the application of a hybrid ML–assisted optimization framework that improves convergence, accuracy, and solution diversity. These results demonstrate the practical potential of biogas-fueled multigeneration systems for sustainable urban energy management and provide a foundation for future research into dynamic operation strategies, integration with other renewable sources, and uncertainty-aware optimization to further enhance real-world applicability. Based on the conducted work, the main conclusions are drawn as follows:

- The CC temperature was the most influential decision variable, with a mean sensitivity index of 0.463, showing the largest impact on efficiencies, sustainability index, and cost indicators, except for net electricity output. The AB pressure ratio ranked second, followed by methane molar fraction, MSC high pressure, and degassing range.
- Higher methane content in the biogas improved power and cooling productivity, exergy efficiency, and the sustainability index. At the same time, it reduced TUPC and increased NPV, demonstrating the importance of fuel quality in system feasibility and supporting methane enrichment as an effective strategy.
- Moderate air blower pressure ratios enhanced exergy efficiency and SI, but higher ratios reduced power and cooling outputs while increasing TUPC and investment costs, ultimately lowering NPV. An optimal operational window was identified where exergetic sustainability and economic viability were balanced.
- Increasing the CC temperature consistently improved thermodynamic and sustainability. Economic performance, however, showed an optimal range of 1400–1450 K, where TUPC was minimized and NPV peaked. Beyond this, economic feasibility declined despite continued efficiency gains.
- Raising high pressure in the MSC cycle improved electricity generation but reduced cooling capacity, creating a trade-off between power and refrigeration. Exergy efficiency and SI increased slightly, while thermal efficiency declined. Economically, the system became more favorable with reduced TUPC and higher NPV, making it suitable when electricity was prioritized.
- The main influence of degassing range was on cooling capacity and thermal efficiency, while electricity generation, costs, and NPV remained almost unchanged. This parameter was most effective as a fine-tuning control for cooling-demand-oriented applications.
- The optimization results showed that the TOPSIS-selected optimum point achieved balanced performance, with TUPC of 26.5 $/GJ, NPV of 13.03 M$, and SI of 1.765. Compared to the base case, TUPC decreased by 10.2%, while NPV and SI increased by 3.7% and 1.1%, respectively, demonstrating improved economic and sustainability outcomes.
- Exergy and exergoeconomic analysis revealed that turbines and the combustion chamber were the largest sources of exergy destruction and cost, while the rectifier exhibited a high cost destruction rate despite low exergy flow. These findings emphasized the need for targeted component-level improvements.
- The long-term economic assessment showed that, over a 20-year lifetime, the optimized case significantly improved financial viability compared to the base mode, with a higher NPV and a shorter payback period (3.79 vs. 4.91 years).
- The optimized system achieved CO emissions of 0.00151 g/kg fuel, NOx emissions of 6.2×10^{-9} g/kg fuel, and a CO_2ER of 1.048 kg/kWh.

The following topics are suggested for future research topics:

- Implementing the proposed biogas-based CCP configuration at pilot or demonstration scale would allow validation of thermodynamic predictions, economic metrics, and long-term operational stability.
- The performance of the soft-computing optimizer may be further improved by employing deep learning, reinforcement learning, or surrogate-based models to enable real-time control and adaptive decision-making.
- Future works can analysis the integration of life-cycle assessment (LCA) and exergoenvironmental indicators to quantify broader environmental impacts.
- Applying the proposed framework to different biogas sources, plant capacities, and industrial or district-energy scenarios would assess scalability and generalizability across diverse energy systems.

CRediT authorship contribution statement

Zhongkui Zhang: Methodology, Conceptualization. **Ling Yao:** Investigation, Formal analysis. **Khalid Alkhattabi:** Investigation, Data curation. **Omar J. Alkhatib:** Writing – review & editing, Validation, Supervision, Data curation. **Ashit Kumar Dutta:** Writing – original draft, Resources, Formal analysis. **Hind Albalawi:** Project administration, Funding acquisition. **H. Elhosiny Ali:** Investigation, Funding acquisition, Formal analysis. **Ibrahim Mahariq:** Writing – review &

editing, Supervision, Investigation, Formal analysis.

Declaration of competing interest

The authors declare that they have no known competing financial interests or personal relationships that could have appeared to influence the work reported in this paper.

Acknowledgement

The authors extend their appreciation to University Higher Education Fund for funding this research work under Research Support Program for Central Labs at King Khalid University through the project number CL/RP/8. Princess Nourah bint Abdulrahman University Researchers Supporting Project number (PNURSP2026R29), Princess Nourah bint Abdulrahman University, Riyadh, Saudi Arabia. Ashit Kumar Dutta would like to thanks AlMaarefa University for supporting this research under project number MHIRSP2025017

Data availability

Data will be made available on request.

References

[1] S.S. Laleh, H.S.R. Mousavi, S. Rabet, F. Nojavan, M. Yari, S. Soltani, Solar thermal assisted proton exchange membrane electrolyzer and solid oxide fuel cell system based on biomass gasification for green power and hydrogen production: multi-objective optimization and exergoeconomic analysis, Energy Convers. Manag. 337 (2025) 119900.
[2] G. Li, J. Xu, S. Liu, D. Zhao, Y. Zheng, W. Guo, High-energy density micro swirl combustion powered thermoelectric generator for combined heat and power supply, Therm. Sci. Eng. Prog. 104369 (2025).
[3] Y. Bi, G. Xia, C. Wang, M. Peng, Y. Xu, J. Wu, Design and transient analysis of a novel type passive residual heat removal system, Nucl. Eng. Des. 445 (2025) 114446.
[4] D. He, H. Li, R. Gao, Y. Li, L. Fan, X. Long, X. Liu, INSL-FLASH: a fission response function based low-cost adaptive reactor physics code for high-Fidelity simulation, Nucl. Sci. Eng. (2025) 1–19.
[5] S. Rabet, S.S. Laleh, O. Habibi, S.A.S. Jahanshahi, M. Yari, S. Soltani, A novel multi-generation system integrating thermophotovoltaic and SOFC system for power and green hydrogen with CO2 liquefaction: a techno-economic and multi-objective optimization study, Fuel 405 (2026) 136581.
[6] Arashrad, P., Sharafi Laleh, S., Rabet, S., Yari, M., Soltani, S., & Rosen, M. A. (2025). Real-time modeling of a solar-driven power plant with green hydrogen, electricity, and fresh water production: techno-economics and optimization. Sustainability (2071–1050), 17(8).
[7] A. Safarpour, S.S. Laleh, S. Soltani, Identifying challenges, benefits, and recommendations for utilizing solar panels in sport stadiums: a thematic analysis, Prog. Eng. Sci. 2 (1) (2025) 100035.
[8] N. Scarlat, J.F. Dallemand, F. Fahl, Biogas: developments and perspectives in Europe, Renew. Energy 129 (2018) 457–472.
[9] M. Pöschl, S. Ward, P. Owende, Evaluation of energy efficiency of various biogas production and utilization pathways, Appl. Energy 87 (11) (2010) 3305–3321.
[10] A. Kalinichenko, V. Havrysh, V. Perebyynis, Evaluation of biogas production and usage potential, Ecol. Chem. Eng. 23 (3) (2016) 387.
[11] M.A. Haghghi, M. Feili, H. Ghaebi, H. Athari, Multi-criteria study and machine learning optimization of a novel heat integration for combined electricity, heat, and hydrogen production: application of biogas-fueled S-Graz plant and biogas steam reforming, Case Stud. Therm. Eng. 63 (2024) 105323.
[12] M. Arslan, C. Yılmaz, Design and optimization of multigeneration biogas power plant using waste heat recovery system: a case study with energy, exergy, and thermoeconomic approach of power, cooling and heating, Fuel 324 (2022) 124779.
[13] J. Castley, U. Azimov, M. Combrinck, L. Xing, Modeling and optimization of combined cooling, heating and power systems with integrated biogas upgrading, Appl. Therm. Eng. 210 (2022) 118329.
[14] M. Ebadollahi, O. Pourali, H. Ghaebi, M. Amidpour, Thermodynamic, economic and environmental study of a combined power generation cycle using biogas fuel as a primary heat source, in: Synergy Development in Renewables Assisted Multi-Carrier Systems, Springer International Publishing, Cham, 2022, pp. 83–106.
[15] P.L. Hervé, T.T. Michael, N.E.P. Salomon, K. Joseph, M.K. Raphael, N. Jean, Energy and exergy analyses of CCHP (combined cooling, heating and power) system based on co-firing of biogas and syngas produced from biomass, Heliyon 9 (11) (2023).
[16] K. Anand, A.P. Mittal, B. Kumar, Cost-inclusive heuristic power management of hybrid power generation plant with ANN-regulated biogas plant, Sustain. Cities Soc. 97 (2023) 104770.
[17] H. Tian, X. Chen, S.F. Ahmad, M.K. Agrawal, A.H. Seikh, N.A. Shah, Q. Su, Modeling and 4E analysis of a new combined cooling, heating, and power energy system based on biogas combustion and hot oil for heat supply, Process. Saf. Environ. Prot. 184 (2024) 1484–1501.
[18] T. Gholizadeh, H. Ghiasirad, S. Rostami, A. Skorek-Osikowska, A biogas-fired cogeneration (cooling and power) system combined with biomethane facilities: 3E evaluation, sensitivity analyses and optimization, Environ. Dev. Sustain. (2024) 1–53.
[19] Z. Huang, B. Su, Y. Wang, S. Yuan, Y. Huang, L. Li, Z. Chen, A novel biogas-driven CCHP system based on chemical reinjection, Energy 297 (2024) 131238.
[20] M.A. Haghghi, M. Feili, P. Nourani, A.M. Bahman, An intelligent NSGA-II-based optimization of a novel biogas-fed oxyfuel gas turbine cycle using CO2 capture option coupled with a multi-heat recovery network and a multi-effect desalination cycle, Desalination 612 (2025) 118957.
[21] M. Feili, H. Ghaebi, M.A. Haghghi, Data-driven optimization of an innovative environmentally friendly power-methanol co-production system utilizing biogas-driven S-Graz cycle, biogas steam reforming, and CO2 capture-hydrogenation process, Renew. Energy 123835 (2025).
[22] H. Athari, S. Soltani, M.A. Rosen, S.M.S. Mahmoudi, T. Morosuk, A comparative exergoeconomic evaluation of biomass post-firing and co-firing combined power plants, Biofuels 8 (1) (2017) 1–15.
[23] N.N. Qeshmi, A.M. Lavasani, M. Vahabi, M. Nimafar, Optimization and techno-economic-environmental assessments of a biomass-powered multi-generation plant for hydrogen and freshwater production, Renew. Energy 240 (2025) 122216.
[24] S.S. Laleh, S. Rabet, H.S.R. Mousavi, M. Yari, S. Soltani, A.S. Mehr, Techno-economic optimization of an integrated ammonia–methane synthesis system powered by LNG-assisted biogas oxy-fuel cycle and vanadium chloride hydrogen production, Energy 138380 (2025).
[25] S. Rabet, S.M.S. Mahmoudi, M. Yari, S. Soltani, Dual-combustion chamber cycle utilizing biomass and geothermal energy: a comprehensive economic analysis and multi-objective optimization for enhanced multi-generation, Renew. Energy 244 (2025) 122760.
[26] D. Kong, X. Tian, G. Li, C. Liu, X. Niu, S.A. Isaev, O.G. Penyazkov, Numerical study of particle deposition and heat transfer characteristics in an S-shaped miniature cooling channel of a gas turbine blade, Powder Technol. 121612 (2025).
[27] L. Ye, H. Guo, Y. Zhu, P. Jiang, Large eddy simulation of film cooling flow from diffusion slot hole with crossflow coolant configuration, Phys. Fluids 35 (5) (2023).
[28] L. Ye, T. Zheng, X. Wang, X. Liang, C. Liu, Evaluating the heat transfer characteristics of mesh-fed slot cooling configuration: influence of slot height and pin-fin arrangement, Appl. Therm. Eng. 271 (2025) 126304.
[29] C. Duan, X. Bai, Y. Tang, Z. Wang, C. Liu, Numerical study on the cooling characteristic of a novel laminated cooling configuration with chained beam turbulator in an afterburner heat shield, Int. Commun. Heat Mass Transf. 167 (2025) 109256.
[30] M. Baghalnezhad, G. Salehi, A.M. Lavasani, M. Vahabi, M. Nimafar, Decision study and optimization of an innovative three-state multigeneration process using solar energy and compressed air energy storage: a data-driven scenario, Appl. Therm. Eng. 256 (2024) 124069.
[31] A. Pacheco-Reyes, W. Rivera, Thermodynamic cycles for the simultaneous production of power and cooling: a comprehensive review, Int. J. Energy Res. 45 (9) (2021) 12500–12535.
[32] A.S. Mehr, M. Yari, S.M.S. Mahmoudi, A. Soroureddin, A comparative study on the GAX based absorption refrigeration systems: SGAX, GAXH and GAX-E, Appl. Therm. Eng. 44 (2012) 29–38.
[33] K.R. Braga Martins, J.R. Figueiredo, Computational simulation and optimization methodology of an ammonia–water GAX absorption cooling system, J. Braz. Soc. Mech. Sci. Eng. 41 (11) (2019) 507.
[34] M.A. Haghghi, M. Shamsaiee, S.G. Holagh, A. Chitsaz, M.A. Rosen, Thermodynamic, exergoeconomic, and environmental evaluation of a new multi-generation system driven by a molten carbonate fuel cell for production of cooling, heating, electricity, and freshwater, Energy Convers. Manag. 199 (2019) 112040.
[35] A. Salehi, S. Mousavi, A. Fasihfar, M. Ravanbakhsh, Thermo-environmental analysis of a new molten carbonate fuel cell-based tri-generation plant using Stirling engine, generator absorber exchanger and vapour absorption refrigeration: a comparative study, Int. J. Hydrog. Energy 46 (77) (2021) 38451–38468.
[36] M. Seiiedhoseiny, L. Khani, M. Mohammadpourfard, G.G. Akkurt, Exergoeconomic analysis and optimization of a high-efficient multi-generation system powered by Sabalan (Savalan) geothermal power plant including branched GAX cycle and electrolyzer unit, Energy Convers. Manag. 268 (2022) 115996.
[37] T. Jia, P. Dou, E. Chen, Y. Dai, Feasibility and performance analysis of a hybrid GAX-based absorption-compression heat pump system for space heating in extremely cold climate conditions, Energy 242 (2022) 122936.
[38] C.P. Jawahar, Simulation studies on GAX based absorption cooling and power cycle using a mixture of ammonia-water working fluid and aluminium oxide nano particles, Mater. Today Proc. (2023), https://doi.org/10.1016/j.matpr.2023.06.120.
[39] F. Jabari, B. Mohammadi-Ivatloo, M.-B. Bannae-Sharifian, H. Ghaebi, Design and performance investigation of a biogas fueled combined cooling and power generation system, Energy Convers. Manag. 169 (2018) 371–382.
[40] C. Xia, Y. Zhu, S. Zhou, H. Peng, Y. Feng, W. Zhou, et al., Simulation study on transient performance of a marine engine matched with high-pressure SCR system, Int. J. Engine Res. 14680874221084052 (2022).
[41] S.A. Kholghi, S.M.S. Mahmoudi, Energy and exergy analysis of a modified absorption cycle: a comparative study, Sustain. Energy Technol. Assess. 32 (2019) 19–28.

[42] A.S. Mehr, V. Zare, S. Mahmoudi, Standard GAX versus hybrid GAX absorption refrigeration cycle: from the viewpoint of thermoeconomics, Energy Convers. Manag. 76 (2013) 68–82.
[43] S. Hou, Y. Wu, Y. Zhou, L. Yu, Performance analysis of the combined supercritical CO2 recompression and regenerative cycle used in waste heat recovery of marine gas turbine, Energy Convers. Manag. 151 (2017) 73–85.
[44] I. Dincer, M.A. Rosen, Exergy: Energy, Environment and Sustainable Development, Newnes, 2012.
[45] H. Athari, F. Kiasatmanesh, M.A. Haghghi, F. Teymourzadeh, H. Yagoublou, M. Delpisheh, Investigation of an auxiliary option to meet local energy demand via an innovative small-scale geothermal-driven system; a seasonal analysis, J. Build. Eng. 50 (2022) 103902.
[46] A. Bejan, G. Tsatsaronis, M.J. Moran, Thermal Design and Optimization, John Wiley & Sons, 1995.
[47] Q. Meng, Y. He, S. Hussain, J. Lu, J.M. Guerrero, Low carbon optimization for wind integrated power systems with carbon capture and energy storage under carbon pricing, Sci. Rep. 15 (1) (2025) 32714.
[48] S. Mohtaram, H. Sun, J. Lin, W. Chen, Y. Sun, Multi-objective evolutionary optimization & 4E analysis of a bulky combined cycle power plant by CO2/CO/NOx reduction and cost controlling targets, Renew. Sust. Energ. Rev. 128 (2020) 109898.
[49] Z. Miao, X. Meng, X. Li, B. Liang, Influence weights of key parameters and optimization strategies for non-contact thermoelectric generator performance enhancement, Energy 339 (2025) 139120.
[50] Y. Gao, M. Tahir, P. Siano, S. Hussain, W. Sun, Y. He, Q. Meng, A bi-level hybrid game framework for stochastic robust optimization in multi-integrated energy microgrids, Sustain. Energy Grids Netw. (2025) 102024.
[51] A. Vakili, A. Pourzangbar, M.M. Ettefagh, M.A. Haghghi, Optimal control strategy for enhancing energy efficiency of Pelamis wave energy converter: a Simulink-based simulation approach, Renew. Energy Focus 53 (2025) 100685.
[52] I. Dincer, M.A. Rosen, P. Ahmadi, Optimization of Energy Systems, John Wiley & Sons, 2017.
[53] K. Ukoba, K.O. Olatunji, E. Adeoye, T.C. Jen, D.M. Madyira, Optimizing renewable energy systems through artificial intelligence: review and future prospects, Energy Environ. 35 (7) (2024) 3833–3879.
[54] A. Ranganathan, The levenberg-marquardt algorithm, Tutor. LM Algorith. 11 (1) (2004) 101–110.
[55] J. Zupan, Introduction to artificial neural network (ANN) methods: what they are and how to use them, Acta Chim. Slov. 41 (3) (1994) 327.
[56] K. Deb, A. Pratap, S. Agarwal, T.A.M.T. Meyarivan, A fast and elitist multiobjective genetic algorithm: NSGA-II, IEEE Trans. Evol. Comput. 6 (2) (2002) 182–197.
[57] M.A. Haghghi, Z. Mohammadi, M. Delpisheh, E. Nadimi, H. Athari, Multi-variable study/optimization of a novel geothermal-driven poly-generation system: application of a soft-computing intelligent procedure and MOGWO, Process. Saf. Environ. Prot. 171 (2023) 507–531.
[58] T. Gholizadeh, M. Vajdi, H. Rostamzadeh, Exergoeconomic optimization of a new trigeneration system driven by biogas for power, cooling, and freshwater production, Energy Convers. Manag. 205 (2020) 112417.